NeuroImage 273 (2023) 120091

Contents lists available at ScienceDirect

NeuroImage

journal homepage: www.elsevier.com/locate/neuroimage

Automatic quality control of the numerical accuracy of EEG lead fields

Usama Riaz[a,#,*], Fuleah A Razzaq[a,#], Ariosky Areces-Gonzalez[a,c,#], Maria Carla Piastra[d], Maria L. Bringas Vega[a,b], Deirel Paz-Linares[a,*], Pedro A. Valdés-Sosa[a,b,*]

[a] The Clinical Hospital of Chengdu Brain Sciences, University of Electronic Science and Technology of China, Chengdu, China
[b] Cuban Neuroscience Center, Havana, Cuba
[c] Department of Informatics, University of Pinar del Rio Hermanos Saiz Montes de Oca, Cuba
[d] Clinical Neurophysiology group, University of Twente, Netherlands

ARTICLE INFO

Keywords:
EEG
BEM
FEM
Lead field
Automated quality control
Item response theory

ABSTRACT

Precise individualized EEG source localization is predicated on having accurate subject-specific Lead Fields (LFs) obtained from their Magnetic Resonance Images (MRI). LF calculation is a complex process involving several error-prone steps that start with obtaining a realistic head model from the MRI and finalizing with computationally expensive solvers such as the Boundary Element Method (BEM) or Finite Element Method (FEM). Current Big-Data applications require the calculation of batches of hundreds or thousands of LFs. LF. Quality Control is conventionally checked subjectively by experts, a procedure not feasible in practice for larger batches. To facilitate this step, we introduce the Lead Field Automatic-Quality Control Index (LF-AQI) that flags LF with potential errors. We base our LF-AQI on the assumption that LFs obtained from simpler head models, i.e., the homogeneous head model LF (HHM-LF) or spherical head model LF (SHM-LF), deviate only moderately from a "good" realistic test LF. Since these simpler LFs are easier to compute and check for errors, they may serve as "reference LF" to detect anomalous realistic test LF. We investigated this assumption by comparing correlation-based channel $\rho_{\min}(ref, test)$and source $\tau_{\min}(ref, test)$ similarity indices (SI) between "gold standards," i.e., very accurate FEM and BEM LFs, and the proposed references (HHM-LF and SHM-LF). Surprisingly we found that the most uncomplicated possible reference, HHM-LF had high SI values with the gold standards—leading us to explore further use of the channel $\rho_{\min}(HHM-LF, test)$and source $\tau_{\min}(HHM-LF, test)$ $_{\text{SI as a basis for}}$ our LF-AQI. Indeed, these SI successfully detected five simulated scenarios of LFs artifacts. This result encouraged us to evaluate the SI on a large dataset and thus define our LF-AQI. We thus computed the SI of 1251 LFs obtained from the Child Mind Institute (CMI) MRI dataset. When $\rho_{\min}(HHM-LF, test)$and source $\tau_{\min}(HHM-LF, test)$ were plotted for all test subjects on a 2D space, most were tightly clustered around the median of a high similarity centroid (HSC), except for a smaller proportion of outliers. We define the LF-AQI for a given LF as the log Euclidean distance between its SI and the HSC median. To automatically detect outliers, the threshold is at the 90th percentile of the CMI LF-AQIs (-0.9755). LF-AQI greater than this threshold flag individual LF to be checked. The robustness of this LF-AQI screening was checked by repeated out-of-sample validation. Strikingly, minor corrections in reprocessing the flagged cases eliminated their status as outliers. Furthermore, the "doubtful" labels assigned by LF-AQI were validated by neuroscience students using a Likert scale questionnaire designed to manually check the LF's quality. Item Response Theory (IRT) analysis was applied to the questionnaire results to compute an optimized model and a latent variable θ for that model. A linear mixed model (LMM) between the θ and LF-AQI resulted in an effect with a Cohen's d value of 1.3 and a p-value <0.001, thus validating the correspondence of LF-AQI with the visual quality control. We provide an open-source pipeline to implement both LF calculation and its quality control to allow further evaluation of our index.

* Corresponding authors.
E-mail addresses: usama.riazahmad@outlook.com (U. Riaz), fuleah.razzaq@outlook.com (F.A. Razzaq), ariosky@neuroinformatics-collaboratory.org (A. Areces-Gonzalez), deirel.paz@neuroinformatics-collaboratory.org (D. Paz-Linares), Pedro.valdes@neuroinformatics-collaboratory.org (P.A. Valdés-Sosa).
# Contributed equally as first authors

https://doi.org/10.1016/j.neuroimage.2023.120091.
Received 22 September 2021; Received in revised form 22 March 2023; Accepted 4 April 2023
Available online 13 April 2023.

1. Introduction

Electroencephalographic (EEG) Source Imaging (ESI) is a widely used neuroimaging modality (Michel et al., 2004) that estimates the primary current sources that generate the observed electrophysiological signals. This estimation is an inverse problem based on the corresponding forward problem defined by the **EEG Lead Field** (**LF**), a continuous linear operator that maps the primary current to the observed activity of "leads"[1].

This operator maps the brain's primary current density, also known as source or generator current density, into the electric potential that is observed at the sensors Eq. (1).

$$v(\mathbf{r}_s, t) = \iint\!\!\!\int \mathbf{k}(\mathbf{r}_s, \mathbf{r}_g) \cdot i(\mathbf{r}_g, t) dV_{\mathbf{r}_g} \tag{1}$$

where the dynamic scalar field $v(\mathbf{r}_s, t) \in \mathbb{R}$at the sensors' spatial domain $\forall \mathbf{r}_s \in \mathbb{R}^3$and in the time domain t describes the electric potential (in Volt's units); the dynamic vector field $i(\mathbf{r}_g, t) \in \mathbb{R}^3$at the sources' spatial domain $\forall \mathbf{r}_g \in \mathbb{R}^3$ and in the time domain t describes the primary current density (in units of Amp/m^3); and the "leads" $\mathbf{k}(\mathbf{r}_s, \mathbf{r}_g) \in \mathbb{R}^3$, for each sensor $\mathbf{r}_s$ a vector field in the sources' spatial domain $\forall \mathbf{r}_g \in \mathbb{R}^3$ describes the ELF (in Ohm's units). The LF depends on the properties of the head as a volume conductor and is usually derived from the quasistatic version of Maxwell's equations (Nunez, P. L., and Srinivasan, 2006) (see section 4.2, 5.6) (Kn and Haueisen, 2022) (see section 5.1.2.5).

Selecting a set of Ns electrodes and then defining Ng sources at fixed brain positions originates a discretization known as the LF operator. This operator is an Ns x Ng x 3 **LF tensor (multidimensional array) K**, Rows $\mathbf{K}(:, \mathrm{j}, \mathrm{k})$ and columns $\mathbf{K}(i, :, \mathrm{k})$, are indexed by the leads and sources, respectively. The tubes $\mathbf{K}(i, \mathrm{j}, :)$ are known as the "Lead Vectors" (LV) of lead I, for source j. The set of all LVs for a given lead is its Lead Vector Field (LVF) K(i,:,:), and its plot is the LVF plot for that lead.

The voltage difference at a given lead of any source dipole inside the volume conductor is the dot product of the LV and the dipole (Malmivuo, 2000). These LVs are the local operators that transforms a unit current source into a lead voltage difference. Thus each LVs are the component along each cartesian axis of the unit dipole forward operators (UDFO), projecting the location and direction of a single dipole with unit strength on an EEG lead (Kn and Haueisen, 2022).

Any ESI estimation technique's accuracy depends crucially on the correctness of the Forward problem. Unfortunately, one does not know the actual LF tensor for a given subject, which has to be estimated from data. Obtaining an individualized LF involves three critical steps: 1) MRI segmentation and artifact removal, 2) realistic head modeling (volume conductor model), and 3) LF computation. Some basic theory about the forward problem is contained in Appendix 10.1 and 10.3. Information about the inverse problem and its dependency on the LF is mentioned in Appendix 10.3.

The uncertainty in this estimation has two primary sources. The first source is the volume conduction model's specification, including the head tissue geometry and conductance definition. Initial simplistic volume conductor models were spherical, being sets of nested spheres, each with a known conductance (Spherical Head Model LF) **SHM-LF**. An even simpler model is a brain floating in an infinite pool with the same conductance (Homogeneous Head Model LF) **HHM-LF**. These simplistic volume conductor models have been superseded by increasingly sophisticated ones that use patient-specific images (such as MRI) to achieve high fidelity. The second source of uncertainty is the actual calculation of the LF tensor from the volume conductor model. Simplistic models that led to LF produce closed analytical expressions that are very accurate (Nolte and Dassios, 2005; Nunez and Srinivasan, 2006). The more realistic models require a more elaborate numerical procedure that may be less tolerant of slight misspecification of the volume conductor.

We underscore the importance of accurate LF matrices for ESI as illustrated in Fig. 1, which is based on Helmholtz's reciprocity principle (Helmholtz, 1876; Malmivuo, 1995, 2000),which states (for a given lead): "the lead field is identical to the electric current field that arises int the volume conductor if a unit current, called reciprocal current $I_R$is fed to the lead " as discussed in (Malmivuo, 2000) (page 5, section 16.2) and in their Fig. 16.1 "RECIPROCITY". This reference clarifies that I_R is obtained by imposing a given voltage V_L at that lead.[2] Thus, if we impose a unit reference voltage difference only at the lead being studied and zero elsewhere, we will induce in the volume conductor, a vector field proportional to that of the Lead Vectors. Consequently, any reasonable inverse solution should reconstruct, from the unit voltage, a vector filed proportional to the LVF PLOT.

Now to Fig. 1. The top row shows LVF PLOTs corresponding to the electrode F10-average reference lead) throughout the volume conductor model.[3] On the left is an LVF PLOT from an accurate LF obtained from an individual MRI with the OpenMEEG BEM. In the middle is the LVF plots for the LF based on a homogeneous head model– a simplistic head model with a brain assumed in an infinite homogenous conductive medium. For these two LVF plots, as expected from electrostatic theory, the LVs of sources close to the electrode are larger and pointed towards the electrode. The LVF plots from a realistic but artifactual LF is on the right, and this expected pattern is absent.

The consequences of LF accuracy are illustrated in the bottom row of Fig. 1, which contains the minimum norm estimation (MNE) of the LVF plot produced by the unit voltage difference imposed at electrode F10. We can see on the left that LVF plot for an accurate LF (on the top) is proportional to the MNE estimate of the LVF plot on the bottom—decreasing with the distance from the electrode and pointing towards it. This statement holds up surprisingly well for the homogenous lead field model in the middle. The LVF plots and their MNE estimate for an artifactual lead field do not correspond to electrostatic theory.

Quality control of individual LFs is thus crucial for the validity of ESI. However, this process is only partially automatic and relies heavily on subjective judgment. This dependence on user intervention becomes a limiting factor when creating LFs with automated pipelines applied to extensive databases. With the availability of High-Performance Computing (HPC) setups, it is common to see LFs computed in bulk or batches for large datasets with 100 s and 1000s of MRIs. Manual inspection of this process is time-consuming, taking days or weeks. Thus, automated, efficient quality control methods for all three steps are needed for working with large datasets, an objective that has only been partially achieved (Michel et al., 2004; Schirner, Rothmeier, Jirsa, McIntosh, and Ritter, 2015).

The first step of LF calculation is segmenting the MRI to define primary brain structures and other tissue boundaries and volumes from the individual MRI, as shown in Fig. 2a. Robust algorithms to distinguish several head tissues, such as the scalp, skull, cerebrospinal fluid (CSF), and gray and white matter, are currently available (Clarke et al., 1995; Despotović, Goossens, and Philips, 2015; Heckemann, Hajnal, Aljabar, Rueckert, and Hammers, 2006). These techniques are available in popular toolboxes such as FreeSurfer (Fischl, 2012), FSL (Jenkinson, Beckmann, Behrens, Woolrich, and Smith, 2012), and Ciftify (Dickie et al., 2018), where, before the segmentation, MRI artifact removal is carried out. MRI segmentations are compared to standard segmented brain MRIs (IBSR, 2013) or assessed by clinical experts (Despotović et al., 2015).

[1] Leads are voltage differences between the activity recorded in two electrodes (V1-VR). In ESI, VR is common to all leads (Hu, Yao, Bringas-Vega, Qin, & Valdes-Sosa, 2019), and we use the terms "lead" and "electrode" interchangeably.

[2] We note that In Malmivou's explanation his notation differs from ours, his $\overline{J}_L(i, j, k)$ are our $K(i, j, k)$

[3] According to the 10/10 electrode system. Also known as the channel E1 in 128 Channel EGI Hydrocel Sensor Nets, supplied by electrical geodesics, https://www.egi.com/research-division/geodesic-sensor-net

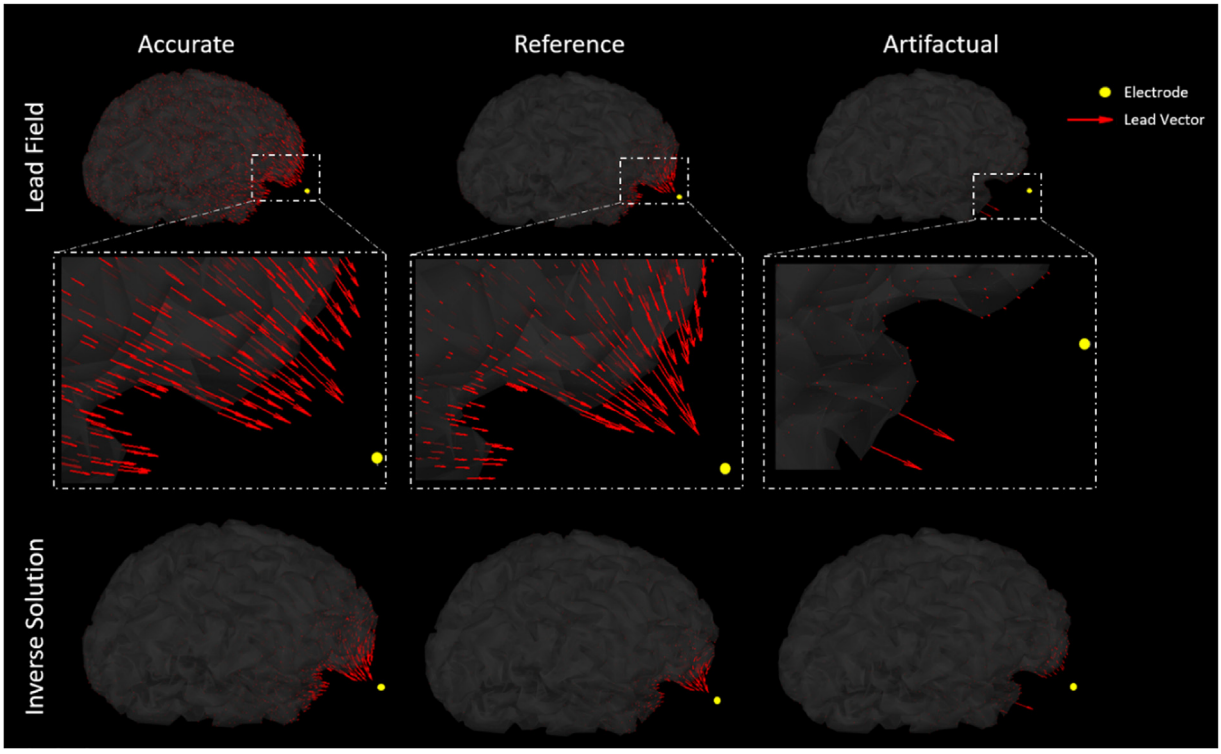

Fig. 1. Comparison of LVF plots and MNE estimates are 3-D visualizations of magnitudes for 8002 sources obtained with LF with different accuracies. All The LVF plots in the top Row shows the lead field vectors for the electrode F10 (the inset in the middle row shows the LVF plots in greater detail). The MNE estimation in the bottom row shows the inverse solution (minimum norm) for a unit voltage at F10.). The vectors are in red and the electrode F10 is a yellow dot. From left to right the columns correspond to accurate, simplistic, and artifactual LFs. The realistic LF was computed from BEM numerical calculations with an accurate head model (OpenMEEG toolbox) with a 3-shell BEM head model with conductivity values set at 0.33, 0.0042, and 0.33. The middle column corresponds to an analytically computed LF, calculated from a simplistic homogeneous head model. The right column is for an artifactual LF produced in a similar way to the accurate lead field but with a head segmentation that produces numerical instability It is evident that a good quality Lead Field results in LVF plot and MNE estimation that are proportional, decrease in strength with distance to the electrode. An artifactual LF lacks these properties. Note that vector lengths represent magnitude. The number of sources was chosen relatively small for visualization purposes only, numerical analysis was with a larger number (287,682).

The model proposed by (Heckemann et al., 2006) to check the quality of MRI segmentation still requires some manual intervention.

The second step, as shown in Fig. 2b, uses the tissue segmentation of step 1 to construct discretized head models and surface and volume mesh for the boundary element method (BEM) and finite element method (FEM), respectively. This step must ensure the necessary conditions for stability in BEM and FEM computations. Realistic volume conductor and source head models are obtained using the tissues extracted from MRI segmentation and the correct alignment of electrodes on the head. Several toolboxes implement this step, such as BrainVISA (Geffroy et al., 2011), EEGLAB-NFT (Delorme and Makeig, 2004), OpenMEEG (Gramfort, Papadopoulo, Olivi, and Clerc, 2010; A. 2011), MNE (Gramfort et al., 2014), Brainstorm (Mosher et al., n.d.; Tadel, Baillet, Mosher, Pantazis, and Leahy, 2011), also the latest FEM calculators, DUNEuro (Schrader et al., 2021a) and FieldTrip (Oostenveld, Fries, Maris, and Schoffelen, 2011; Vorwerk, Oostenveld, Piastra, Magyari, and Wolters, 2018a). Unfortunately, although they may include some built-in quality control criteria, discretization methods within these tools always require manual tuning (Jas et al., 2018; Vorwerk, Aydin, Wolters, and Butson, 2019).

The third step uses the meshes constructed from step 2 to carry out the numerical calculation of LFs (Fig. 2c), for which there exist accurate and state-of-the-art methods (A. Gramfort et al., 2011; Medani et al., 2021a). There are several methods for computing the LF. In most BEM implementations, the LFs are computed with head models defined by concentric compartments with homogeneous conductivity. These compartments are enclosed surfaces with defined surface potentials. An example of a three-compartment model comprises the cortex, inner skull, and outer skull (Akalin Acar and Makeig, 2013; Ermer, Mosher, Baillet, and Leahy, 2001; Fuchs, Kastner, Wagner, Hawes, and Ebersole, 2002; Huang, Mosher, and Leahy, 1999; Mosher, Leahy, and Lewis, 1993, 1999; Opitz, Paulus, Will, Antunes, and Thielscher, 2018; Rahmouni, Adrian, Cools, and Andriulli, 2019; Vatta, Meneghini, Esposito, Mininel, and Di Salle, 2010). BEM is relatively fast and can be used with increasingly sophisticated models as one adds different compartments. Nevertheless, for greater realism, the Finite Element Method (FEM) uses 3D meshes (Dannhauer, Brooks, Tucker, and MacLeod, 2012; M. Dannhauer, Lanfer, Wolters, and Knösche, 2011; Hallez et al., 2007; Nolte and Dassios, 2005; Piastra et al., 2020; Vorwerk et al., 2014, 2018a; Windhoff, Opitz, and Thielscher, 2013; Yamaguchi, 2014). FEM can deal with inhomogeneous and anisotropic conductivities but requires a higher computational burden. Both these procedures are available in several toolboxes, i.e., BrainVISA (Geffroy et al., 2011), EEGLAB-NFT (Delorme and Makeig, 2004), OpenMEEG (Gramfort et al., 2010; A. 2011), MNE (Gramfort et al., 2014), Brainstorm (Mosher et al., n.d.; Tadel et al., 2011). The latest FEM calculators are DUNEuro (Schrader et al., 2021b) and FieldTrip (Oostenveld et al., 2011; Vorwerk et al., 2018a). We note that there are other, less used LF calculation methods, such as the Finite Difference method (FDM) (Cuartas Morales, Acosta-Medina, Castellanos-Dominguez, and Mantini, 2019; Hallez et al., 2007; Vatta et al., 2010) and finite volume method (FVM) (Cook and Koles, 2006; Grant and Lowery, 2009; Xie, Yuan, Xinshan, and Guan, 2001) which are not dealt in this paper.

Although methods for step 3 are very accurate, they may depend critically on the correctness of the previous two stages. Quality control of

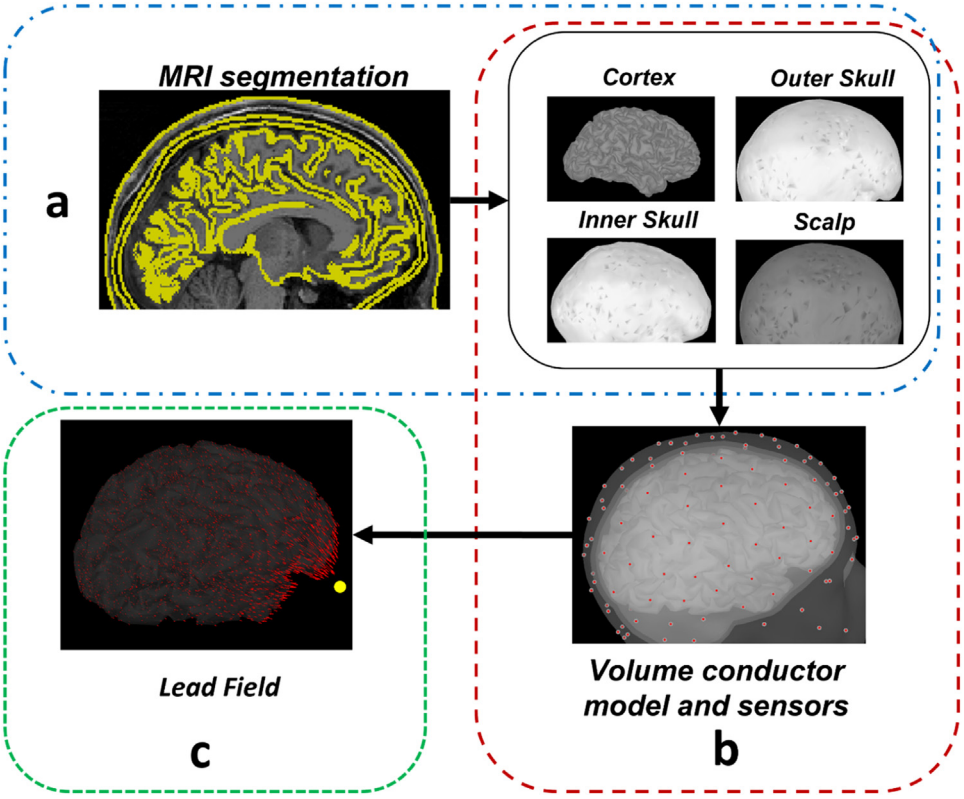

Fig. 2. Forward model shown in three steps. **(a)** First step (MRI segmentation), which extracts different brain and non-brain tissues. In this case FreeSurfer was used to extract the cortex and FSL was used to extract inner and outer skull along with scalp. **(b)** Realistic head model is generated by generating BEM or FEM meshes for extracted tissues and combining them with proper alignment. In this case BEM meshes were generated to create head model. This step also includes accurate alignment and placement of electrodes on the scalp. **(c)** Visualization of the Lead Field for channel F10 is shown on the cortex. In this case LF was computed using OpenMEEG BEM.

the final result of the whole process has received little attention, despite its importance for correct EEG source localization. Checking the overall correctness of the LF is the focus of our attention in this paper. To date, such quality control also requires human evaluation of some criteria for the source distribution of LF orientations and amplitudes (Mosher et al., 1993, 1999; Nunez, P. L., and Srinivasan, 2006; Vatta et al., 2010).

BEM and FEM are complex numerical procedures that are error-prone since they depend on the conductivity profiles and (possibly) the anisotropic nature of different tissues between sources and electrodes. These may lead to numerical instabilities. To date quality of BEM or FEM is checked by manual inspection (Mosher et al., 1993, 1999; Nunez, P. L., and Srinivasan, 2006; Vatta et al., 2010). This manual technique for quality control is even more time-consuming than the first two steps of LF calculation and, therefore, quite impractical for extensive data sets. There have been a preliminary study in this context (Vega et al., 2021).

We propose a novel measure, the Lead Field Automatic-Quality Control Index (LF-AQI), to facilitate quality control of the numerical computations of extensive LF datasets. Our LF-AQI is based on the following premise: we assume that the BEM or FEM "test" LF, as shown in Fig. 1 (first column), is roughly like a more simplistic "reference" LF shown in Fig. 1 (middle column), which can be calculated analytically, thus eliminating the possibility of numerical inaccuracies shown in Fig. 1 (third column). The reference LF, though less accurate, is assumed to be sufficiently like the test LF to allow its use for screening. The simplest possible Lead-Field (Nunez, P. L., and Srinivasan, 2006), which we adopt as a reference, is the HHM-LF, as also shown in Fig. 3c.

In other words, we assume that each test LF in the dataset should be only a moderate transformation of reference head model LF. This transformation might vary depending on the complexity of the head model, but the two LFs should be correlated to each other when compared numerically. The similarity of test and reference LF is measured by the channel and source-wise Pearson correlation between two LFs. If an LF does not have any numerical computational errors, the correlation values and LF-AQI should be high, with low values indicating LF with problems.

To test this assumption on correlations between test and reference LF, we analyze different types of LFs, Spherical, BEM, and FEM, comparing them with a highly realistic model that includes anisotropy (Piastra et al., 2020). Based on these comparisons, we analyze how correlations change in simulated artifactual LFs, which leads us to define the LF-AQI. Finally, we verify the utility of our index by analyzing a large MRI dataset. The LF-AQI evaluation of this dataset is then compared with manual quality control. A description of the associated open-source pipelines is also given.

2. Materials and methods

In what follows, we employ the following mathematical notation. Lowercase letters denote scalars, e.g., x. Lowercase bold letters denote column vectors, e.g., $\mathbf{x} \in \Re^n$with n the number of rows. Upper case bold letters denote matrices, e.g., $\mathbf{X} \in \Re^{n\times m}$ with m the number of columns. Elements of a vector or matrix are scalars denoted with the same letter as the object of which they are a part and with subindices indicating the component referred to, e.g., x_i and $x_{i,j}$. $\mathbf{x} \cdot \mathbf{y}$ denotes the scalar product of these vectors. $|\mathbf{x}| = \sqrt{\mathbf{x} \cdot \mathbf{x}}$ is the norm of a vector. Table 1 shows the explanations of different symbols in the paper.

2.1. Lead fields studied

The head modeling comprises three components. These are

- The volume conduction or head model specifies all head compartments for brain and non-brain tissues. It also assigns conductivity values to these compartments. For BEM models, these conductivities are constant within each compartment, and only the surfaces separating them are required. For FEM models, the conductivities are

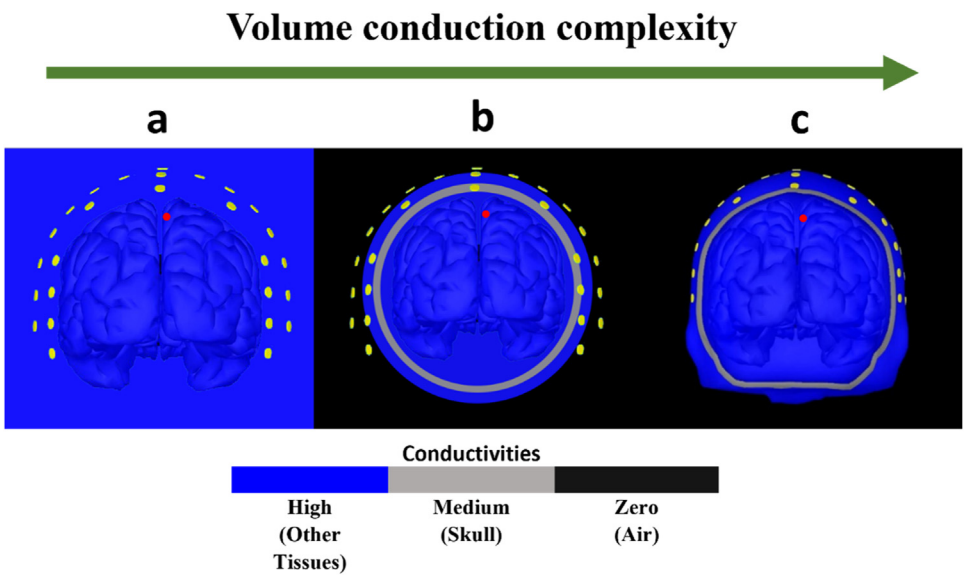

Fig. 3. a) HHM-LF K_{hom}, which is computed via fully analytical methods in a boundary-free volume conductor model and with constant conductivity defined as an average in head tissue. b) Spherical LF $\mathbf{K}^{sp}$, which is computed via stable semi-analytical methods employing a spherical approximation of the piecewise volume conductor model of the head, which also includes the skull. c) BEM LF $\mathbf{K}^{BEM}$ in a moderately detailed piecewise conductor model extracted from a segmentation of the MRI and including the skull.

Table 1
Symbols used in the paper and their explanation.

Symbol	Acronym	Description
	UDFO	A unit dipole forward operator
	LV	Lead Vector
$\mathbf{K}$	LF	Lead field tensor or matrix
N_c, N_s,N_i	–	Number of channels, sources, and individuals
$\mathbf{K}^{test} \in \Re^{Nc \times Ns}$	Test	$test_i$ LF of subject i
$\mathbf{K}^{ref}\Re^{Nc \times Ns}$	Ref	Reference head model LF ref_i of subject i
$\mathbf{K}^{\text{hom}}$	HHM-LF	Homogenous head model LF
$\mathbf{K}^{sp}$	SHM-LF	Spherical head model LF
$\mathbf{K}^{BEM}$	BEM	Boundary Element Method LF
$\mathbf{K}^{FEM}$	FEM	Finite Element Method LF
K^{3c}	FEM,3c	FEM LF, 3 tissue head model
K^{4c}	FEM,4c	FEM LF, 4 tissue head model
K^{6c}	Fem,6c	FEM LF. 6 tissue head model, Gold standard LF
$\mathbf{K}^{art}$	art	Simulated Artifactual LF
$\rho(c; ref, test)$	CSP	Channel Similarity Profile (Correlations)
$\rho_{\min}(ref, test)$	CSI	Channel Similarity Index (Minimum correlation)
$\tau(s; ref, test)$	SSP	Source Similarity Profile (Correlations)
$\tau_{\min}(ref, test)$	SSI	Source Similarity Index (Minimum correlation)
$(\vartheta_{channel}, \vartheta_{sourece})$	HSC	High Similarity Centroid (Median of CSI and SSI)

specified for each component of a volume tessellation. When considering anisotropic conductivity, each component has a conductivity tensor of a scalar value.

- As the introduction mentions, the general discretized Lead Field $\mathbf{K}$ is a tensor with rows $\mathbf{K}(:,j,k)$, columns $\mathbf{K}(i,:,k)$, and tubes $\mathbf{K}(:,:,k)$. However, in this paper, we project the tensor's Lead Vectors (tubes) onto the $\boldsymbol{\mu}_s$, the unit vector, which is normal to the cortex. The tube $\mathbf{K}(:,:,k)$ is substituted by $\mathbf{K}(:,:,k) \cdot \boldsymbol{\mu}_s$, transforming the tensor into a matrix, with the rows and columns of this matrix representing projected lead and sources, respectively, with the dimensions $N_c \times N_s$. Note that we retain the same matrix symbol as the tensor.
- The Electrode positions $\mathbf{y}_c, c = 1, \cdots, Nc$and the sources are specified by each source's location $\mathbf{x}_s$, $s = 1, \cdots, Ns$

The LF matrices we consider $\mathbf{K} \in \Re^{Nc \times Ns}$ have elements $\{k_{c,s}\}$. Test LF ($\mathbf{K}^{test}$) is the actual lead field to be examined for artifacts. Reference LF ($\mathbf{K}^{ref}$) is the simpler lead field used to screen artifacts in the $\mathbf{K}^{test}$. The different types of $\mathbf{K}^{test}$and $\mathbf{K}^{ref}$ considered in this paper are defined in the following sub-sections (2.2.1–2.2.4). When there is a need to specify the number of individuals used to calculate both reference and test LF, we add the suffix $i = 1, \cdots Ni$.

2.1.1. Homogenous head model lead field

The homogenous head model LF $\mathbf{K}^{\text{hom}}$ is based on a head model with constant conductivity when the brain is in an infinite and homogeneous medium. A visual representation of K^{hm} is shown in Fig. 3-left column, where the blue color codes the uniform connectivity of the head and the infinite surrounding media. This type of LF only depends on the electrode and source coordinate positions while assuming that the brain is placed in an infinite homogeneous medium, as mentioned in Equation 1.7 of the book "Electric Fields of the Brain – The neurophysics of EEG" (Nunez, P. L., and Srinivasan, 2006). With the electrode positions and source model, we have a slightly modified version of this equation:

$$k_{c,s}^{\text{hom}} = \frac{1}{4\pi\sigma_{brain}} \left(\frac{\mathbf{r}_{c,s} \cdot \boldsymbol{\mu}_s}{|\mathbf{r}|^3} \right) \tag{2}$$

Here $\mathbf{r}_{c,s} = \mathbf{y}_c - \mathbf{x}_s$ is the difference vector between the source s and channels c, $\vec{\mu}$ the orientation of the source dipole, and σ_{brain} the homogeneous conductivity similar to the brain, which in this case is constant because of an infinite homogeneous medium, so Eq. (2) can be rewritten as:

$$k_{c,s}^{\text{hom}} = \alpha \frac{\mathbf{r}_{c,s} \cdot \boldsymbol{\mu}_s}{|\mathbf{r}|^3} \tag{3}$$

Where $\alpha = \frac{1}{4\pi\sigma_{brain}}$because the conductivity of the model is constant. Upon analyzing the dataset described in 2.2.4, we found that for the sources close to a specific electrode, the expression in Eq. (3) blows up (details are in the discussion section). Therefore, we placed a variable e in Eq. (3) that limits the effect of $1/|\mathbf{r}|$as shown in Eqs. (4) and 5. After testing several values e, we selected the value ($e = 0.007$ meters) that maximizes the correlation between these theoretical and actual LFs.

$$k_{c,s}^{\text{hom}} = \frac{1}{4\pi\sigma_{brain}} \left(\frac{\mathbf{r}_{c,s} \cdot \boldsymbol{\mu}_s}{\max(|\mathbf{r}|^3, e^3)} \right) \tag{4}$$

$$k_{c,s}^{\text{hom}} = \alpha \frac{\mathbf{r}_{c,s} \cdot \boldsymbol{\mu}_s}{\max(|\mathbf{r}|^3, e^3)} \tag{5}$$

However, Eqs. (4) and 5 are theoretical equations that, for calculation and implementation purposes, Eq. (5) can be written as:

$$k_{c,s}^{\text{hom}} = \alpha \frac{\cos\left(\psi_{c,s}\right)_s}{\max(|\mathbf{r}|^2, e^2)} \tag{6}$$

Here, $\psi_{c,s}$ the angle between $\mathbf{r}_{c,s}$and $\boldsymbol{\mu}_s$.

2.1.2. Spherical head hodel lead field $\mathbf{K}^{sp}$

The spherical head model K^{sp} is more realistic than K^{hm}yet easy to calculate. We estimate the closest fitting spheres from the electrode configuration to obtain this model. Spherical head models compute LFs while assuming the brain is inside one or multiple spheres (3 spheres in our case) with different conductivities, as shown in Fig. 3b. The spherical head models used in this study are from the METH toolbox.[4] The specific head model computed was based on the study of Nolte et al. (Nolte and Dassios, 2005), with conductivities of each sphere set as 0.33, 0.0042, and 0.33 S/m, respectively. The head model and conductivities are visualized in Fig. 3-middle column.

2.1.3. BEM realistic lead fields $\mathbf{K}^{BEM}$

The BEM LFs in this study are computed using the BEM volume conduction model proposed by (Akalin Acar and Makeig, 2013; Ermer et al., 2001; Fuchs et al., 2002; Huang et al., 1999; Mosher et al., 1993, 1999; Vatta et al., 2010). We used the OpenMEEG (Gramfort et al., 2010; A. 2011) toolbox embedded in the Brainstorm software. The conductivity values for the scalp, skull, and brain were set at 0.33, 0.0042, and 0.33 S/m, respectively. These LF matrices have $N_s = 8002$ (number of sources) and $N_c = 129$(number of electrodes).

2.1.4. FEM realistic lead fields $\mathbf{K}^{FEM}$

The FEM LFs used in this study are from Piastra et al., who computed three FEM head models using the DUNEuro toolbox (Medani et al., 2021b; Piastra et al., 2020; Schrader et al., 2021b). The LF matrices for these head models have $N_s = 278621$ and $N_c = 81$. They computed three head models by considering three, four, and six types of brain and non-brain tissues and called them the 3C, 4C, and 6C head models. For this current study, we will refer to these models asK^{3c}, K^{4c}, K^{6c}. This 6C model includes the properties of white matter (anisotropic), gray matter, CSF, skull compacta, skull spongiosa, and scalp. $\mathbf{K}^{FEM,6c}$ is the most detailed and accurate LF in this study and is taken as a gold standard.

2.2. Quantifying the similarities of test and reference lead fields

The similarity profiles between the test LF $\mathbf{K}^{test}$and reference LF $\mathbf{K}^{ref}$ is assessed with two measures based on the Pearson correlation coefficient.

The first measure assesses the Channel Similarity Profile (CSP), which is, for each channel c, the correlation between the values of both types of LF:

$$\rho(c;ref,test) = \frac{\sum_{s=1}^{N_s}\left(k_{c,s}^{ref} - \overline{k_c^{ref}}\right)\left(k_{c,s}^{test} - \overline{k_c^{test}}\right)}{\sqrt{\sum_{s=1}^{N_s}\left(k_{c,s}^{ref} - \overline{k_c^{ref}}\right)^2 \sum_{s=1}^{N_s}\left(k_{c,s}^{test} - \overline{k_c^{test}}\right)^2}} \tag{7}$$

where $\overline{k_c^{test}} = \frac{1}{Ns}\sum_{s=1}^{Ns} k_{c,s}^{test}$and a similar definition for $\overline{k_c^{ref}}$.

The Channel Similarity Profile can be visualized as a topographic plot, as in Fig. 4 (left pane), displaying each channel's correlation value.

The **Channel Similarity Index (CSI)** is defined as $\rho_{\min}(ref,test) = \min_{\forall c} \rho(c;ref,test)$ and summarizes the worst correlations over all channels between reference and test LF.

The second type of similarity profile measure assesses, for each source s, the correlation between the values of both types of LF. A naïve expression would be:

$$\tau_{naive}(s;ref,test) = \frac{\sum_{c=1}^{N_c}\left(k_{c,s}^{ref} - \overline{k_s^{ref}}\right)\left(k_{c,s}^{test} - \overline{k_s^{test}}\right)}{\sqrt{\sum_{c=1}^{N_c}\left(k_{c,s}^{ref} - \overline{k_s^{ref}}\right)^2 \sum_{c=1}^{N_c}\left(k_{c,s}^{test} - \overline{k_s^{test}}\right)^2}} \tag{8}$$

[4] https://www.nitrc.org/projects/meth/

where $\overline{k_s^{test}} = \frac{1}{Nc}\sum_{c=1}^{N_c} k_{c,s}^{test}$and a similar definition for $\overline{k_s^{ref}}$.

However, this variant of the Source Similarity Profile $\tau_{naive}(s;ref,test)$ are correlations calculated with fewer samples than the Channel Similarity Profile. In preliminary calculations, we found that this leads to very variable estimates across sources with an excess of outliers. To decrease correlation variability, we increase the degrees of freedom of the estimator by spatial smoothing of $\tau_{naive}(s;ref,test)$ as a weighted average of the spatially nearest neighbors:

$$\tau(s;ref,test) = \sum_{i\in N(s,dth)}^{k} \omega_i\, \tau_{naive}(i;ref,test) \tag{9}$$

where$N(s,dth)$ is the set of the nearest neighbors of the source $\omega_i = \frac{\mathbf{r}_{i,s}}{\sum_{j\in N(s,k)}^{k}|\mathbf{r}_{j,s}|}$ whose Euclidean distance from $\tau(ref,test) = \min_s rzscore(\overline{\tau}(s;ref,test),1)$ is less than an empirically selected threshold dth(values equal to 20 mm in our case), and $\omega_i = 1 - \frac{|\mathbf{r}_{i,s}|}{\sum_{j\in N(s,k)}^{k}|\mathbf{r}_{j,s}|}$., where $|\mathbf{r}_{i,s}|$ is the distance between a source and its nearest neighbors. The smoothed Source Similarity Profile can be visualized as cortical plots, as in Fig. 4 (right column), displaying each source's correlation value. We found this naïve definition to be susceptible to the presence of outliers. We, therefore, use a robust estimate $\tau(s;ref,test)$, excluding these outliers.[5]

We call this **Source Similarity Index (SSI)** which is denoted as $\tau_{\min}(ref,test)$.

2.3. Simulation of artifactual lead fields

To simulate an artifactual LF, $\mathbf{K}^{art}$ we corrupted the gold standard K_{6c} by adding a large value to specific sets of rows and columns. The reasoning behind this simulation is that the computation of the LF is a complex numerical calculation, iteratively solving high-dimensional linear equations (Gramfort et al., 2010; Medani et al., 2021b; Nolte and Dassios, 2005). When this process does not converge, or the parts of the head model are incorrect, the LF matrix may exhibit substantial values reflecting artifacts (Adjerid and Weinhart, 2011; Bird, Coombs, and Giani, 2019). We found these substantial values by empirically analyzing the set of LFs in this study. These values are one of the many outcomes that reflects artifacts in LFs when linear solvers do not converge. Unfortunately, the tools based on these linear solvers to compute LFs do not return a runtime error when these solvers do not converge. Instead, they either return the most recent value in the iteration and save the specific element $k_{c,s}$ of the LF (OpenMEEG), or the error message has to be visualized manually at the of LF computation (DuNeuro) (Gramfort et al., 2010; Schrader et al., 2021b). Formally the simulations take the form:

$$k_{c,s}^{art} = k_{c,s}^{FEM,6c} + a \forall a \in A \tag{10}$$

Where the set $A = \{-\infty, -1000, -100, -10, -5, -1, 0, 1, 5, 10, 100, 1000, \infty\}$ specifies the values for which we simulated the corrupted parts of the LF matrix. These values were selected empirically for the LFs used in this study. These values are relative to the entries of LF and can be selected from the set A based on the LF being used. The simulation figures used in this paper were generated from the value 100; overall, we tested a set of values from$A$, and they yielded the same outcomes. In this research, we studied 5 scenarios illustrated in Fig. 5.

[5] To select a robust minimum of $\tau(s;ref,test)$ we, select the value of the 1st percentile for all sources. This percentile is found from the distribution of the robust z-scores of the smoothed source correlations: $z_\tau(s;ref,test) = \frac{0.6745(\tau(s;ref,test) - median(\tau(s;ref,test)))}{MAD}$ where Median Absolute Deviation is $MAD = median(|\tau(s;ref,test) - median(\tau(s;ref,test))|)$ (Howell, 2014).

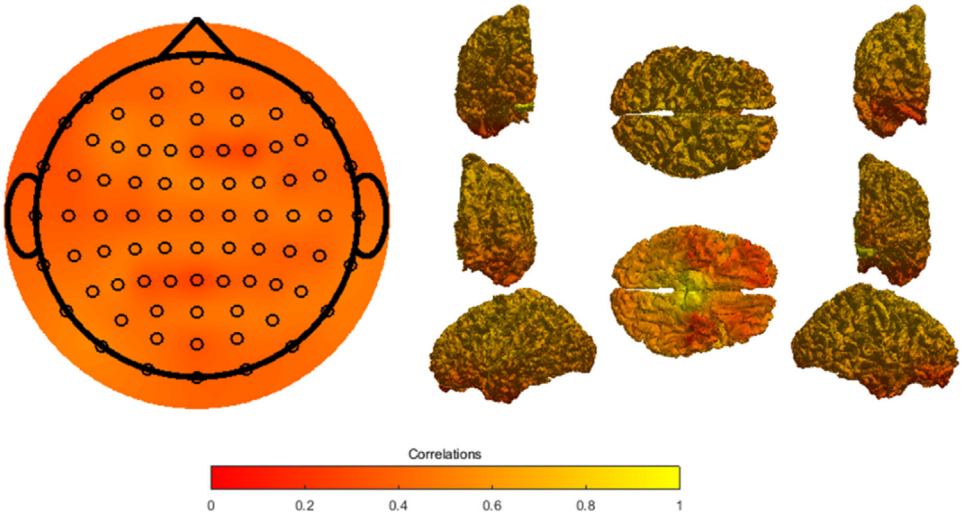

Fig. 4. An example of the channel and source similarity profile between a reference lead field ($\mathbf{K}^{\text{hom}}$) and a test LF ($\mathbf{K}^{FEM,6c}$). Left: Topographic view of the Channel Similarity Profile $\rho(c; ref, test)$. Right: Multiple views of the Source Similarity Profile $\tau(s; ref, test)$.

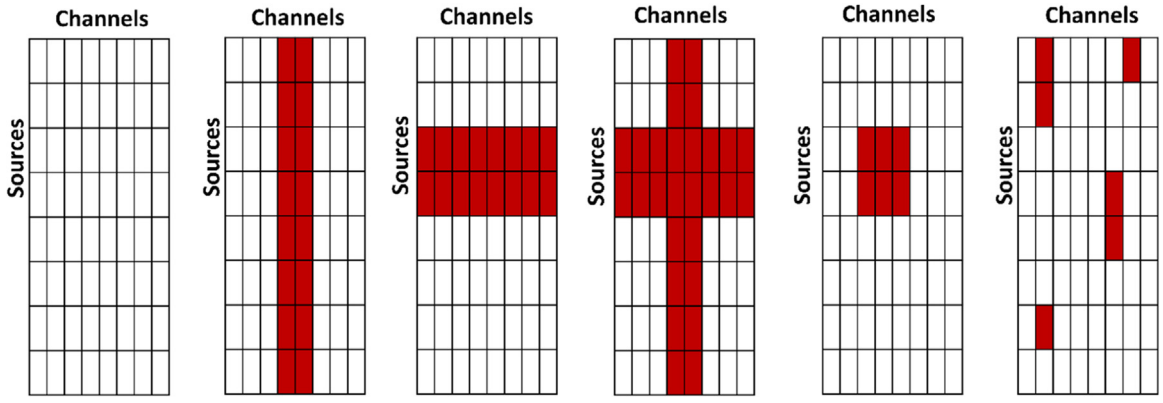

Fig. 5. Five different scenarios in which artifacts are added to the gold standard LFs.

2.4. Analysis of the child mind institute (CMI) mri-eeg dataset

To explore the properties of BEM LFs for a large open-science dataset, we selected the ChildMind Institute (CMI) EEG-MRI repository that contains information from 1251 subjects from the Healthy Brain Network initiative (Alexander et al., 2017). MRIs were collected using Siemens 3T Tim Trio MRI scanner. EEG was a High-Density EEG data recorded using a 128-channel EEG geodesic hydroCel EGI system, available at http://fcon_1000.projects.nitrc.org/indi/cmi_healthy_brain_network/index.html.

Using standard modules, BEM LFs were obtained from all subjects using an in-house pipeline developed at Joint CC-Lab, UESTC, China (Areces-Gonzalez, 2020; Areces-Gonzalez et al., 2023).

This pipeline (shown in Fig. 6) estimates the LF for each subject in three steps 1) HCP structural pipeline, 2) Realistic head model, and 3) LF computation. This pipeline uses functions from HCP structural pipeline (Glasser et al., 2013) based on the FreeSurfer toolbox (Fischl, 2012) and Ciftify (HCP)(Dickie et al., 2018). Later, we computed realistic head models using the built-in BEM functionality of Brainstorm Toolbox (Tadel et al., 2011). In the last step, we computed LFs using OpenMEEG (Gramfort et al., 2010), which uses BEM based volume conduction model for LF computation. We now give more details for each step of the pipeline:

1) In the first step, we processed raw T1 MRI images using the Freesurfer toolbox to perform segmentation, denoising, normalization, and co-registration of different brain and non-brain tissues. In this step, we used the "recon_all" function of the Freesurfer toolbox (Fischl, 2012). The output from the Freesurfer toolbox was given as input to the Ciftify toolbox (Dickie et al., 2018) to convert the Freesurfer directory into the CIFITFY space or HCP format directory (Dickie et al., 2018; Glasser et al., 2013). We applied the same "recon_all" function to get this standard output compatible with the Brainstorm toolbox (Mosher et al., n.d.; Tadel et al., 2011). At the end of this step, we performed a quality check to identify the topological defects and verify the gray matter, white matter, and CSF segmentation.

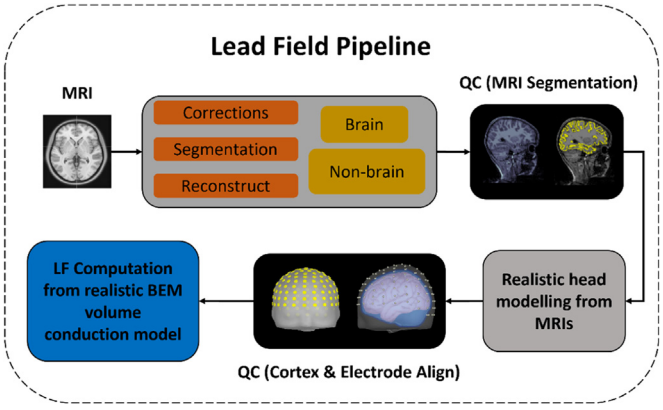

Fig. 6. Pipeline for Lead Field computation explaining the three steps involved, from MRI segmentation to realistic head modeling to LF computation.

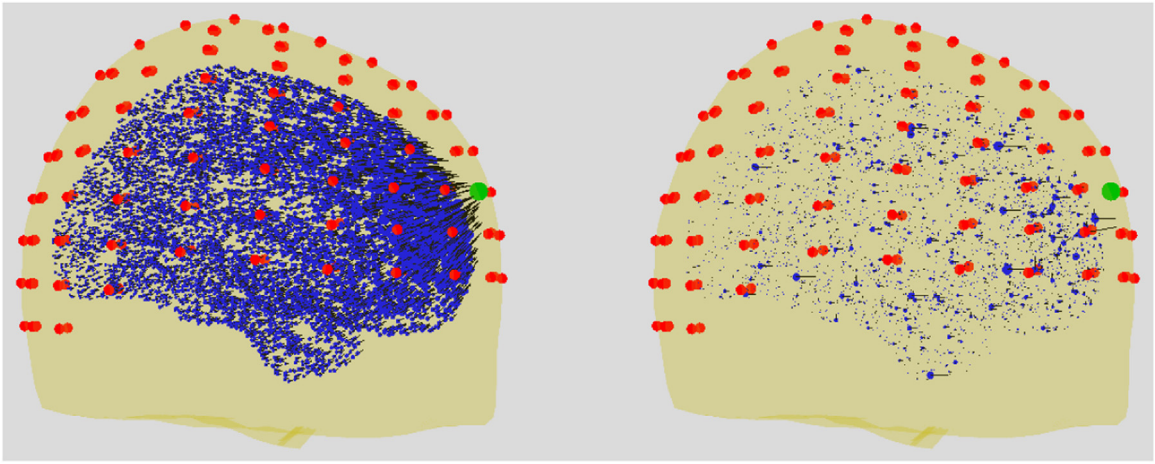

Fig. 7. LVF plot used for manual quality control, (a) good lead field with all LVs pointing towards the EEG sensor under observation (marked by a green circle), and a decay in the magnitude of LVs of all cortical dipole sources. (b) artifactual lead field with no visible magnitude decay or proper direction for the of LVs towards the EEG sensor.

2) Upon verifying the quality of the segmented and co-registered MRIs, we checked if the registration of these MRIs with brain and non-brain tissues was accurate. Next, we computed realistic head models with the scalp, skull, CSF, and cortex surface boundaries using a BEM-based head modeler embedded in Brainstorm. Later, we checked the alignment of the cortex and electrodes with head models.
3) In the end, the BEM volume conduction model proposed by (Akalin Acar and Makeig, 2013; Ermer et al., 2001; Fuchs et al., 2002; Huang et al., 1999; Mosher et al., 1993, 1999; Vatta et al., 2010) was used to compute individual LFs. We used the OpenMEEG (Gramfort et al., 2010; A. 2011) toolbox embedded in the Brainstorm software. Before computing the LFs, the conductivity values must be selected based on the volume conduction model. In this case, the conductivities for Scalp, Skull, and Brain were set at 0.33, 0.0042, and 0.33 S/m, respectively. The eventual LFs have 8002 dipole sources for each individual.

2.5. Manual quality control of lead fields

The LF of all 1251 CMI subjects was subjected to a manual quality control exercise. Towards this end, we first generated LVF plots for all LFs in the dataset. These LVF plots represent each electrode and show the LVs placed at the specific location in the lead. These LVs in the LVF plots should show their direction pointing towards the electrode according to the standard text on electromagnetic signal propagation properties (Malmivuo, 1995, 2000; Nunez, P. L., and Srinivasan, 2006). Its intensity decreases as we move away from the electrode. Following these concepts mentioned in section 16.2 of (Malmivuo, 2000), figure 11.19 of (Malmivuo, 1995), and section 5.6 of (Nunez, P. L., and Srinivasan, 2006), the LVF plots were checked for two main properties:

- The LVs of dipole sources point towards the electrode for which these LVF plots were made
- The size of LVs decreases as the distance of the corresponding dipole source increases from that electrode

Fig. 7 shows two LVF plots for “accepted” (Fig. 7 on the left) and “doubtful” (Fig. 7 on the right) LFs classified by LF-AQI. Red-filled circles represent the EEG sensor location on the scalp, and the green-filled circle is the EEG sensor being observed for the LVF plot. Blue dots show the location of the dipole source on the cortex, and the size of the blue dot and its corresponding arrow shows the strength of LV corresponding to the source, contributing to the eventual voltage measured at the EEG sensor (green-filled circle).

Fourteen evaluators from different educational backgrounds studying Neuroscience at our lab evaluated these LFs. These evaluators analyzed the LVF plots using a questionnaire designed to evaluate the plots based on the theory from the abovementioned books. The questionnaire is available at: (https://docs.google.com/forms/d/1NcQ5tzkGO99ONZetiRLECOzdLBXKNcjvKliFfqMZVtc/edit). Some ite ms in the questionnaire were directly relevant to the quality of the LVF plots, cortex, and electrode alignment with the head model. However, others were irrelevant and included as controls. We requested that the evaluation indicate the level of confidence. The evaluators ranked their answers on a Likert scale of **1–5,** considering one a confident yes response and five a confident no. Though all evaluators did not revise all LFs, we did ensure that every LF was checked by multiple evaluators’ estimates and accounted for evaluator bias. The visual quality control questionnaire is as follows:

Q1 Head, Cortex, and Electrodes are aligned?
Q2 What is the accuracy of LVs pointing toward the EEG sensor?
Q3 How well is the symmetry of decay for the LVs according to their distance from the electrode?
Q4 Based on the above inputs, rate the lead field.
Q5 What is the confidence level of the opinion?
Q6 What was the difficulty level of analyzing the LVF plots for the above questions?

We performed an Item Response Theory (IRT) analysis on the questionnaire results. IRT is a mathematical model that reconstructs a latent factor based on measured items/questions scores when items are categorical and not continuous. The scale for our questionnaire ranges from 1 to 5; thus, we have used a polytomous IRT (Beaujean, 2014; P. Chalmers, 2015). We have used the R package MIRT (R. P. Chalmers, 2012)for this analysis. We constructed a latent factor from the six questions and used a generalized partial credit model (R. P. Chalmers, 2015; Pollitt and Hutchinson, 1987), which implements multiple 2PL models for each adjacent category (Wu, Tam, and Jen, 2016). We tested the IRT model using factor loadings (how well a question is loading on the latent variable, a higher value is better), and item discrimination scores η tell how well a question differentiates between evaluators; larger η indicates high discriminability). Moreover, TRACE plots or Item Response Category Characteristic Curves were used to see if evaluators used all the categories from the scale and if the scale matched the behavior of eval-

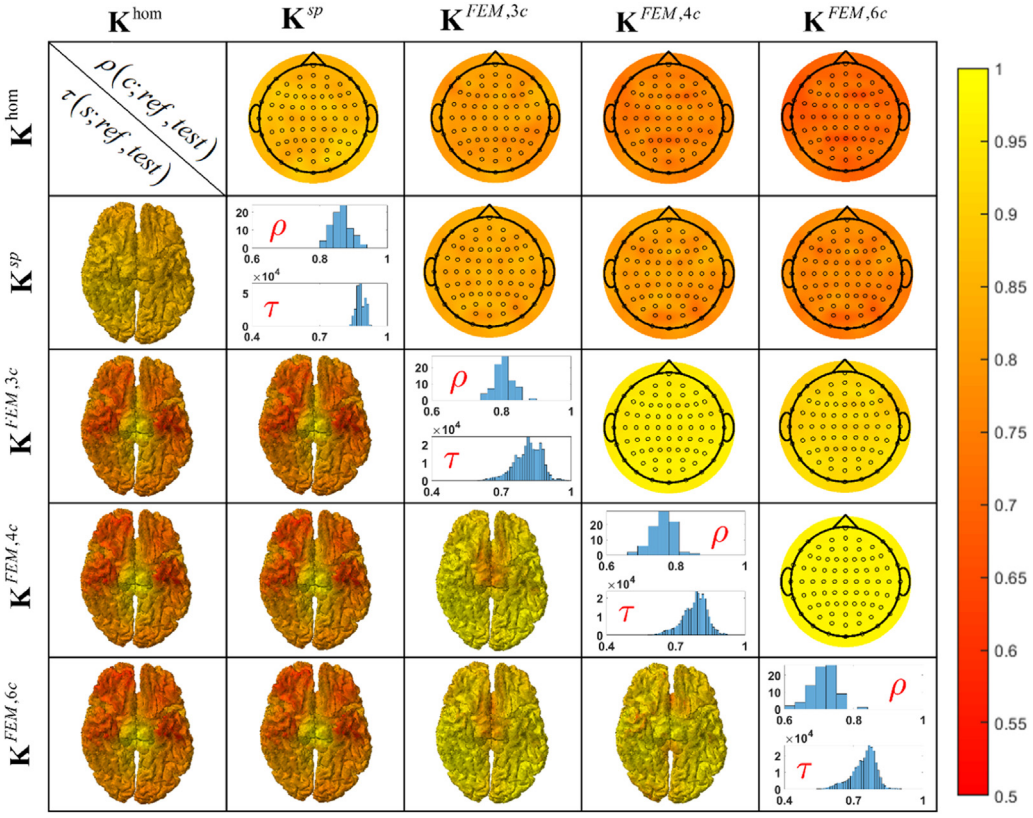

Fig. 8. Channel-wise and Source-wise Correlations between LFs computed from $\mathbf{K}^{hom}$, K^{sp}, $\mathbf{K}^{FEM,3c}$, $\mathbf{K}^{FEM,4c}$ and $\mathbf{K}^{FEM,6c}$LFs. Channel-wise correlations as a topographic map on the head and source-wise as a cortical map.

uators. A good question should show a trace plot where the evaluators use all categories.

We employed all six questions to load onto the latent factor for the initial model. We have analyzed the factor loadings, item discrimination scores, and item trace plots to check if all the answer categories are visible at the theta level θ (latent factor). We then optimized the initial model based on the findings above and compared both models using the R "ANOVA" function (Anderson-Cook, 2007; Fox, 2015; Hand, 1987; O'Brien and Kaiser, 1985). We implemented Akaike's Information Criteria (AIC), Bayesian Information Criteria (BIC), and Log-likelihood as model selection criteria. Based on the AIC and BIC, we selected one of the models and used it to get the latent factor scores for further analysis.

After generating the latent factor scores θ for manual QC using IRT, we compared these scores with automated quality control variables to validate our proposed Quality Index. We implemented multi-level models for repeated measures to describe the relationship between manual QC IRT scores and automated QC variables. The generic notation for multi-level models or linear mixed models (LMMs) is

$$Y = \beta X + \gamma Z + \varepsilon \tag{11}$$

Here Y is the outcome variable, $X$is the fixed effect variable, and a grouping variable $Z$for random effects. $a$and γ are estimated parameters for fixed and random effects, respectively. We applied three LMM models (Eq. (11)) with different outcome variables (Y). The three LMM models were for $\rho_{\min}(ref,test)$, $\tau_{\min}(ref,test)$, and a quality index LF-AQI (defined below). All three variables were scaled using Fisher's z-transform before LMM (Zucker, 1965). Latent manual QC score (θ) was the fixed effect(X), and evaluators were the random effects(Z).

$$Y \sim \theta + random(Evaluators) \tag{12}$$

"**lme**" (Linear, Mixed, Models, Fit, and Hmisc, 2022) function in R was used to estimate the coefficients and p-values for fixed and random terms. Additionally, Cohen's d effect size for LMM was estimated using "**lme.dscore**" function from the EMAtools (Kleiman, 2021). A Cohen's d value of 0.2–0.7 means a small to medium effect size, and a value of 0.8 or greater means a large effect.

3. Results

3.1. Similarity profiles between lead fields with increasing complexity

To see how well LFs with increasing complexity approximate each other, we computed scalp topography of$\rho(c;ref,test)$and the cortical topography of $\tau(s;ref,test)$ between K_{hom}, K_{sp}, K_{3c}, K^{4c} and K^{6c}. Fig. 8 shows a matrix plot for these comparisons. The upper triangle area shows the topographic maps for all $\rho(c;ref,test)$, and the lower triangle shows the posterior view of the cortical map of all $\tau(s;ref,test)$. Only the posterior view is shown for the latter since it had the greatest variability. The detailed cortical view of $\tau(s;ref,test)$ between K_{hom} and K_{6c} was already shown in Fig. 4. The diagonal of the plot shows the histogram of the $\rho(c;hom,test)$and $\tau(s;hom,test)$ for all test LFs. We summarize our findings in Fig. 8 as follows:

- Channel $\rho(c;ref,test)$ and $\tau(s;ref,test)$ Source Similarity Profiles between the different types of lead fields studied in this paper are surprisingly high.
- Both $\rho(c;ref,test)$and $\tau(s;ref,test)$ decreases for more complex head models when HHM-LF is considered reference LF but still give values above 0.6 and 0.5, respectively.
- The similarity profiles comparing all types of realistic lead fields are very high (>0.95)
- Despite being lower than when using realistic LF as a reference, $\rho(c;hom,test)$, $\rho(c;sp,test)$ $\tau(s;hom,test)$ and $\tau(s;sp,test)$are much higher than initially expected, more than 0.6 for channels and 0.5 for sources.

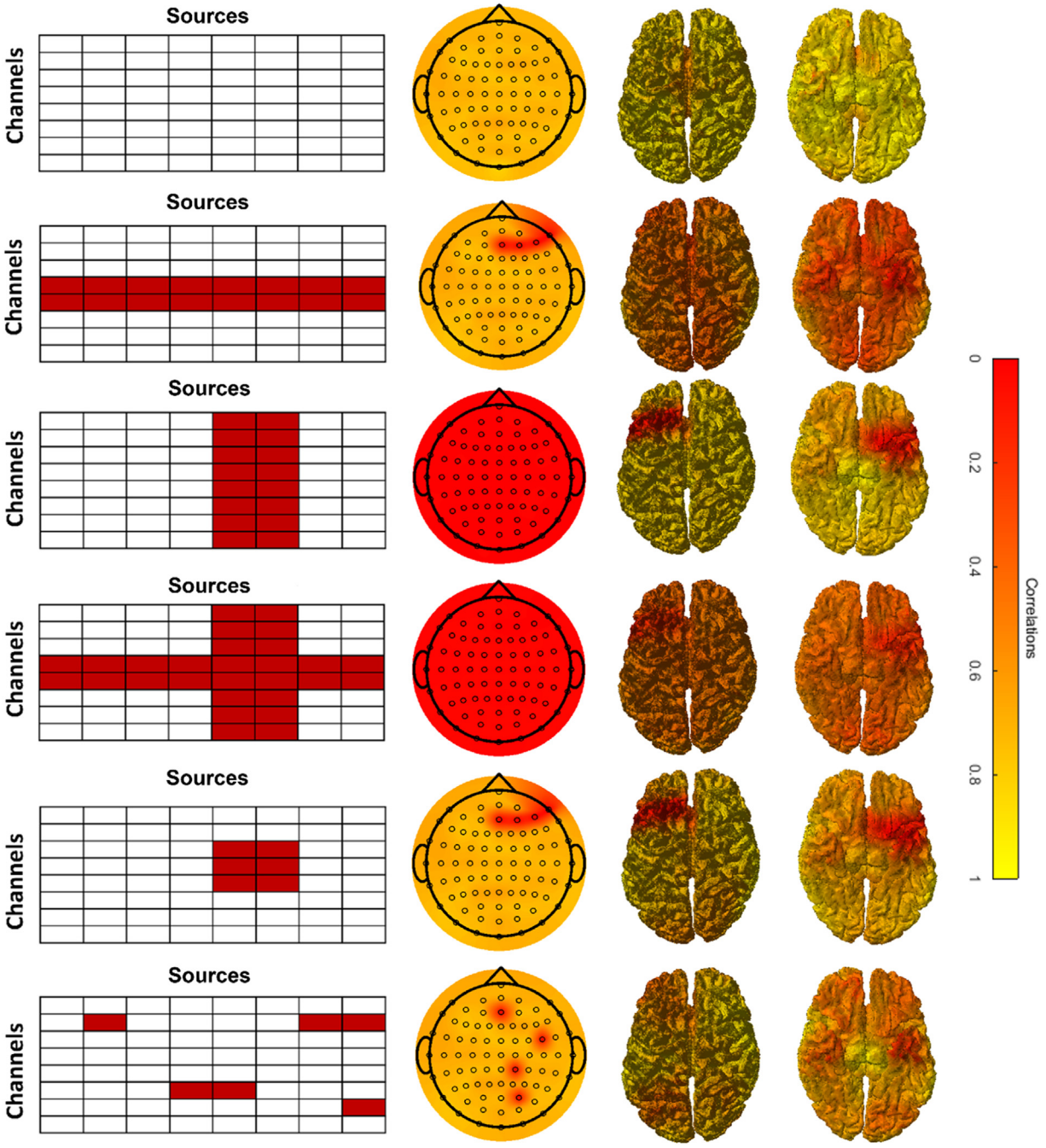

Fig. 9. Sensitivity of similarity profiles to artifactual LFs: The first column shows the artifacts simulated in the LF matrix. The second column shows a topographic map of artifacts on different channels. The third and fourth columns shows cortical maps of artifacts.

The histograms at diagonals also endorse this claim when looking at the summary measures. If we look at histograms from simple LF to complex ones, it is evident that histograms move away from the highest values of the correlation coefficient. However, this value does not go below 0.6 in the case of channels and 0.5 in sources.

Interestingly, both $\rho(c; hom, sp)$ and $\tau(s; hom, sp)$ are remarkably high and have good correlations with the realistic LF, suggesting that either could be used as a computationally inexpensive references. However, K_{hom} can be computed an order of magnitude faster than K_{sp}. We henceforth adopted K_{hom} as the reference LF and searched for an automatic LF quality control index using it.

3.2. Sensitivity of the similarity profiles to artifactual lead fields

We tested five different scenarios to produce noise distortions to assess the sensitivity of channel and Source Similarity Profiles to the simulated "artifactual LF, " as described in Section 3.3. Fig. 9 illustrates the six cases considered (including $\mathbf{K}^{FEM,6c}$), with the corresponding similarity profiles below. These scenarios are (listed here in the order of Fig. 8, from left to right):

1 **No artifact:** $\mathbf{K}^{FEM,6c}$ as taken as a test, LF and compared to the $\mathbf{K}^{hom}$ reference exhibited large channel $\rho(c; hom, sp)$and $\tau(c; hom, sp)$Source Similarity Profiles.

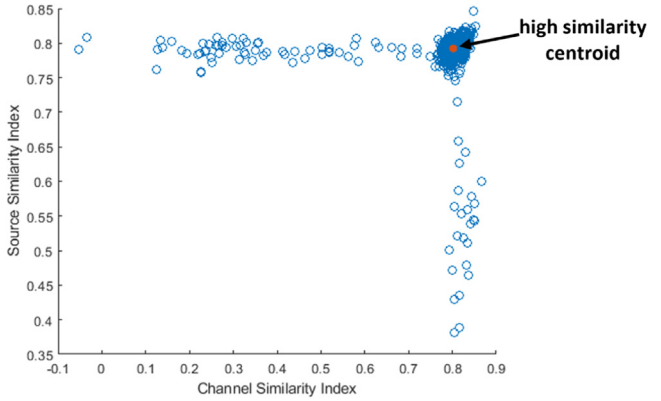

Fig. 10. Scatter plot of the CSI and SSI for all 1251 LFs from the CMI dataset. Note that the cluster of LFs with high similarities has as its centroid (HSC) at (0.80,0.79).

2 **Localized channel artifact**: The expected lower $\rho(c; hom, sp)$values in the Channel Similarity Profile result from corruption in the test LF of all sources for a group of closely spaced channels. This channel-wise artifact also has a widespread decrease in source correlations.
3 **Source region of interest** (ROI) **artifact**: When the sources in the LF corresponding to an ROI in the sources are corrupted across all channels, the cortical similarity profiles plots show low correlations for the specific area in which sources have artifacts. However, the similarity profile across all channels is degraded, as expected.
4 **Combined localized channel cortical ROI artifact**: Corrupting the LF using a blend of scenarios 2. and 3. produces a scalp similarity profile akin to that of the cortical ROI artifact and a Source Similarity Profile akin to that of the localized channel artifact.
5 **Circumscribed channel and source artifact**: In this fifth scenario, the LF is corrupted for a group of adjacent channels belonging to a cortical region of interest. The results on the topographical plots show noise in the channels that have artifacts. Similarly, cortical plots also show artifacts in the area where we only have added noise.
6 **Sparsely distributed artifact:** In the last scenario, simulated sources and channels LF entries have noise added in a sparse pattern. The scalp topographic maps exhibit a random pattern of low values. Cortical plots show low correlations in the patches where we have added simulated noise.

These simulations of artifactual LF show the similarity profiles $\rho(c; ref, test)$and $\tau(s; ref, test)$are sensitive to corruption of a reference lead field, with circumscribed ROI artifacts easily identified.

3.3. Distribution of the similarity indexes across subjects for the cmi bem lf

As described in detail in Section 2.5, we calculated the BEM LF for 1251 HBN subjects from the EEG-MRI repository. A scatter plot of the source Similarity Indices versus Channel Similarity Indices for all subjects are shown in Fig. 10. The scatter plot shows a concentrated cluster of points centered at the point (0.80, 0.79) with straggling horizontal and vertical lines of outliers that indicate possible artifacts for the sources or channel elements of fewer LFs. A reasonable hypothesis is that the cluster corresponds to well-calculated LFs. This idea is the basis for our definition of the Lead Field Automatic Control Index (LF-AQI) proposed in the next section. We shall call the centroid (median of all data points of 1251 LFs) in Fig. 10 the **high similarity centroid (HSC)** and denote it as $(\vartheta_{channel}, \vartheta_{source})$. Its value is (0.80, 0.79) in this sample.

3.4. The lead field automatic-quality control index (LF-AQI)

As seen in the previous section, most of the LFs studies have high Channel and Source Similarity Indices, forming what we have called a high similarity cluster. It is easy to identify the centroid of this cluster which allows us to define our index.

The Lead Field Automatic-Quality Control Index (LF-AQI) is the $\log_{10}$ of Euclidean distance between the HSC and the LF of the individual i to be tested:

$$\mathrm{LF-AQI}_i = \log_{10}\left(\left\|\begin{bmatrix}\rho_{\min}(\mathrm{hom}_i, BEM_i)\\ \tau_{\min}(\mathrm{hom}_i, BEM_i)\end{bmatrix} - \begin{bmatrix}\vartheta_{channel}\\ \vartheta_{source}\end{bmatrix}\right\|_2^2\right) \quad (13)$$

Fig. 11 (top) shows the histogram of the sample LF-AQI. We decided to identify LF-AQI values larger than the 90th percentile as possibly artifactual and needing to be checked. In this particular case, the LFs are the ones that have LF-AQI greater than −0.9755.

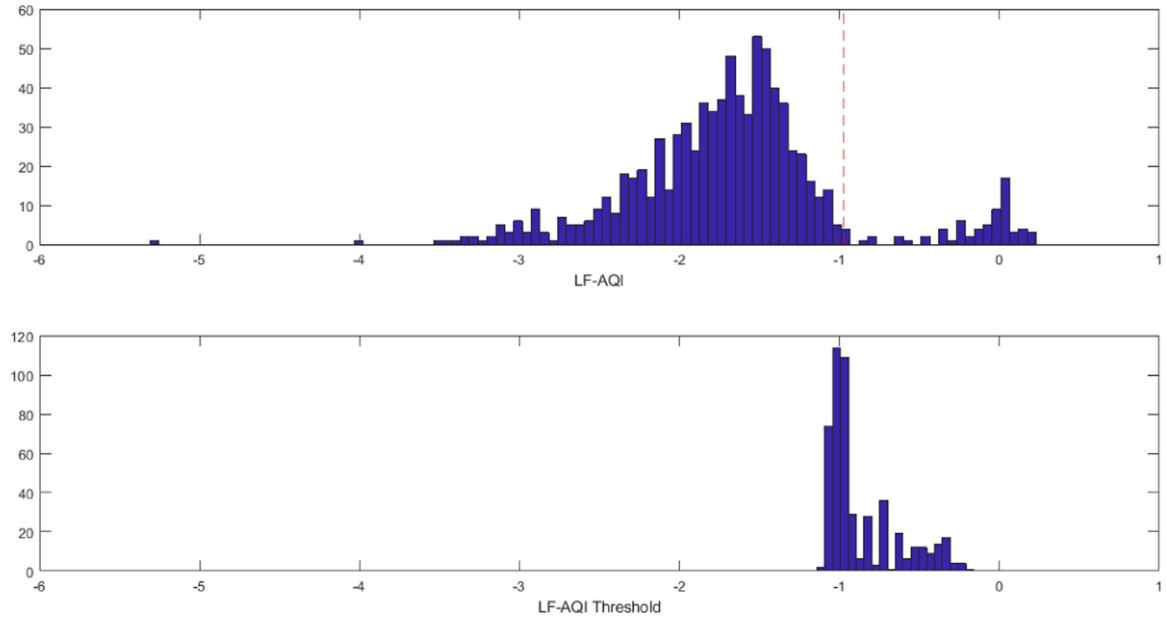

Fig. 11. Top: Histogram of LF-AQI with the threshold for "doubtful" LFs. Bottom: Histogram of LF-AQI threshold of 500 random samples.

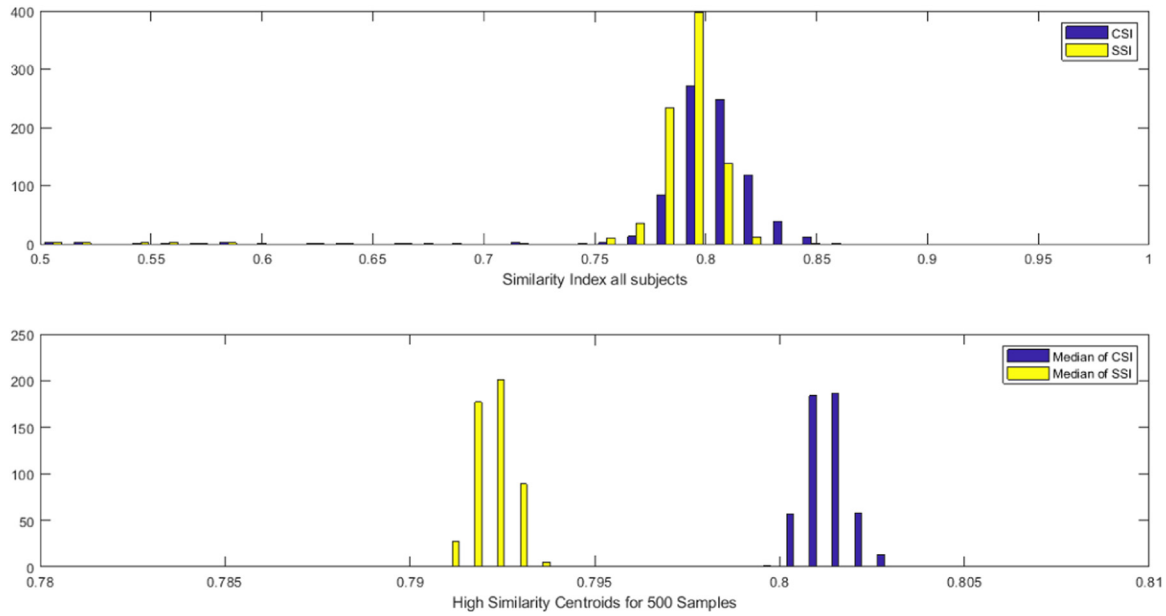

Fig. 12. Top: Histogram of CSI and SSI for 1251 subjects. Bottom: High similarity centroids for 500 random samples shown in a zoomed-in scale between (0.78,0.81).

We used a cross-validation technique to ensure that the HSC, LF-AQI, and threshold have out-of-sample validity. Specifically, we carry out repeatedly the following procedure (500 times):

- Randomly divide the CMI dataset into training and testing sets with a ratio of 50% each
- Obtain an HSC from the training dataset
- Obtain the LF-AQI from the test set

Fig. 11 (bottom) shows the histogram of the LF-AQI threshold from 500 random samples, and it shows that LF-AQI and its thresholds are valid for out-of-sample testing. Similarly, Fig. 12 (top) shows the similarity index for all 1251 subjects, showing most LFs have high values and some LFs have low values of CSI and SSI. Fig. 12 (bottom) shows that high similarity centroids for 500 random samples have almost no variation, and they are around (0.80, 0.79).

3.5. An lf-aqi pipeline

As a result of the developed methods, a pipeline for LF-AQI was created, shown in Fig. 13. The pipeline takes bulk LFs $\mathbf{K}^{test,i}$ produced by standard LF workflows as input. Our pipeline then computes $\mathbf{K}^{hom,i}$ against each LF and computes the CSI and SSI for those LFs. The pipeline then projects these CSI and SSI on a 2D space and computes an HSC by taking the median of CSI and SSI, respectively. Using HSC, it computed the LF-AQI using the formula in Eq. (14). Once LF-AQI is computed, the pipeline tags the LFs as accepted LFs and "doubtful." We then re-analyze MRIs and head models that computed these "doubtful" LFs for corrections.

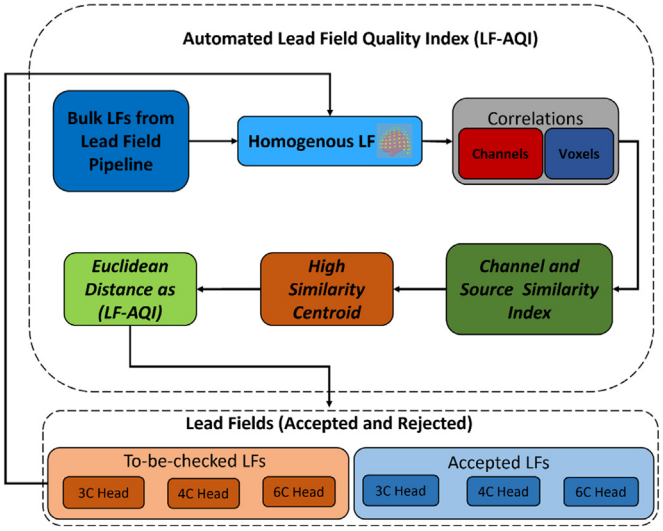

Fig. 13. LF-AQI pipeline showing each step involved in computing and applying LF-AQI on a large dataset.

3.6. Visualizing and correcting the artifacts using the lf-aqi

We analyzed all 60 LFs declared as "doubtful" by the LF-AQI pipeline and 40 LF samples from the 1251 LFs of the CMI dataset. We found three reasons why the LFs were screened as "doubtful":

1 The first reason was the blurred/noisy MRI causing inaccurate segmentation. Fig. 14a shows, as an example, three views of a blurred/noisy MRI in the first row. The second row shows that these MRIs do not produce correct tissue boundaries. Eventually, these result in incorrect tissue segmentation and the reconstructed tissues from the segmentation of these MRIs generate a distorted, "spiky" surface mesh, as shown in the third row. However, Fig. 14b shows another cleaner/smoother MRI (first row), in which the tissue boundaries are identifiable (second row). This MRI produces accurate tissue segmentation and reconstruction, as shown in the third row. Numerical instability emerges in many situations due to the skull layer's close disposition and low conductivity relative to the gray matter sources (Akalin Acar and Makeig, 2013; M. Dannhauer et al., 2011; Vorwerk et al., 2019). Conductivity heterogeneities at the boundary between the scalp and the air may contribute to such numerical instability, but in less measure, since this boundary is more distant to the gray matter

2 Fig. 15a shows an evident misalignment of the cortex inside the head. Thus, the LF computed from this head modeling is also declared "doubtful." Fig. 15b shows a properly aligned cortex without noticeable artifacts; hence, the LF computed from this head model passed the LF-AQI test.

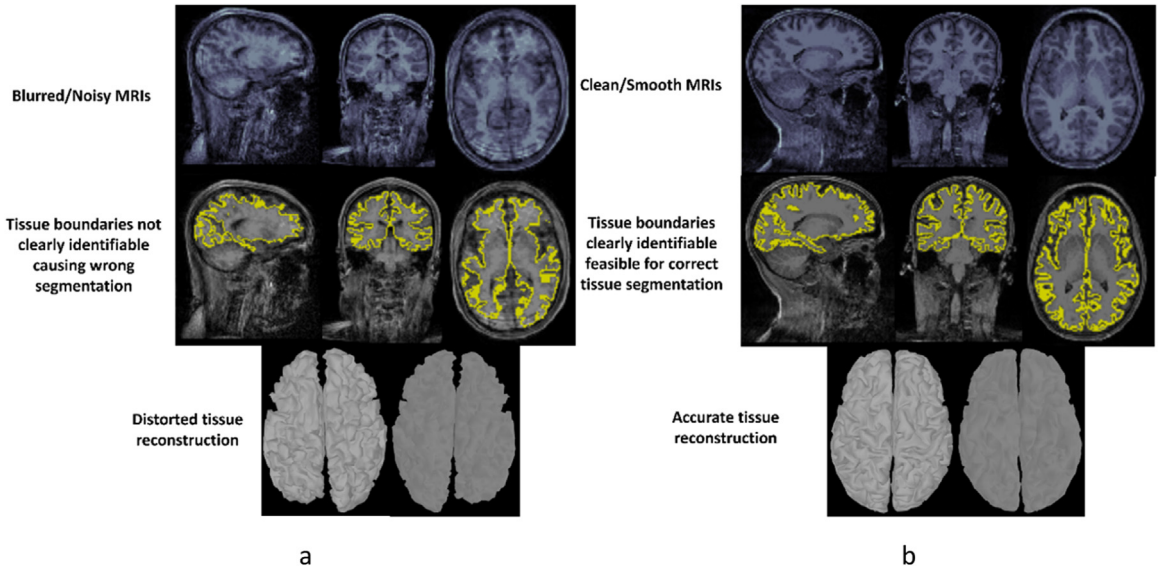

Fig. 14. Degraded MRIs that produce artifactual LF and clean ones. (a) First row: Blurred/Noisy MRI, Second row: Tissue boundaries are not identifiable, causing wrong segmentation, Third row: Due to improper segmentation, tissue reconstruction is distorted. (b) First row: Clean/Smooth MRI, Second row: Tissue boundaries are identifiable, making a basis for accurate segmentation, Third row: Proper segmentation yield accurate tissue segmentation.

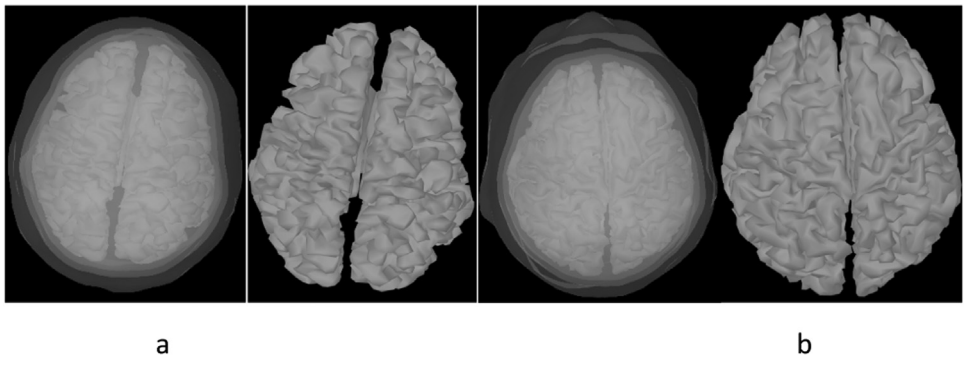

Fig. 15. Cortical alignment with head volume (a) Cortical alignment for an LF declared "doubtful" by LF-AQI. The electro-head alignment is not correct. (b) Cortex alignment of LF was declared accurate by LF-AQI.

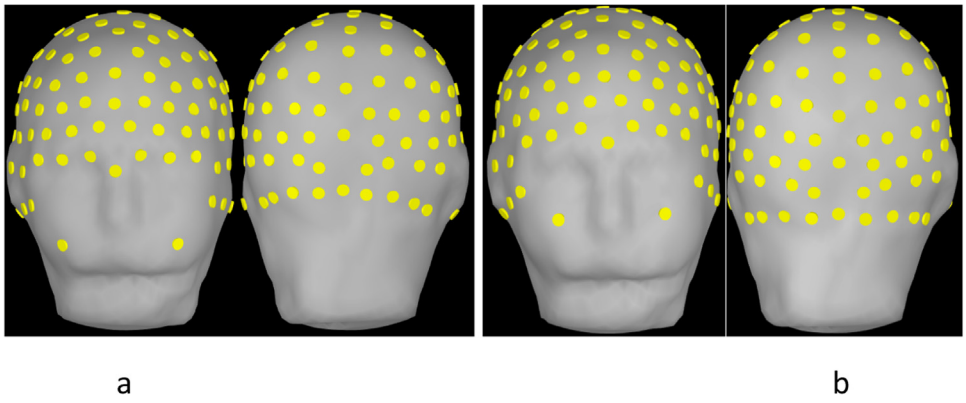

Fig. 16. EEG electrode alignment affects LF quality (a) Electrode alignment of LF declared "doubtful" by LF-AQI. (b) Electrode alignment of LF was declared accurate by LF- AQI.

3 Fig. 16a shows that the LF's electrode alignment with artifacts needs distance correction and realignment. Fig. 16b shows corrected and realigned electrodes on the head.

The next step was removing the mentioned artifacts and recomputing the LFs.

The next step is to remove the mentioned artifacts and compute the LFs again. In case of incorrectly segmented MRIs, we first try to reperform the MRI segmentation steps to achieve proper segmentation. However, in cases where MRIs still cannot be properly segmented, we proceed by substituting HCP structural outputs and FSL nonbrain tissue of an individual subject with chosen template outputs. The templates are useable to perform approximated electrophysiological source imaging from the EEG. A specific parameter in the pipeline configuration files allows switching individualized or predetermined template anatomy to facilitate this process. This feature helps correct the second type of artifact we found in the "to-be-checked" labeled LFs. The last correction is to correct the sensor layout. Since we have already performed auto-

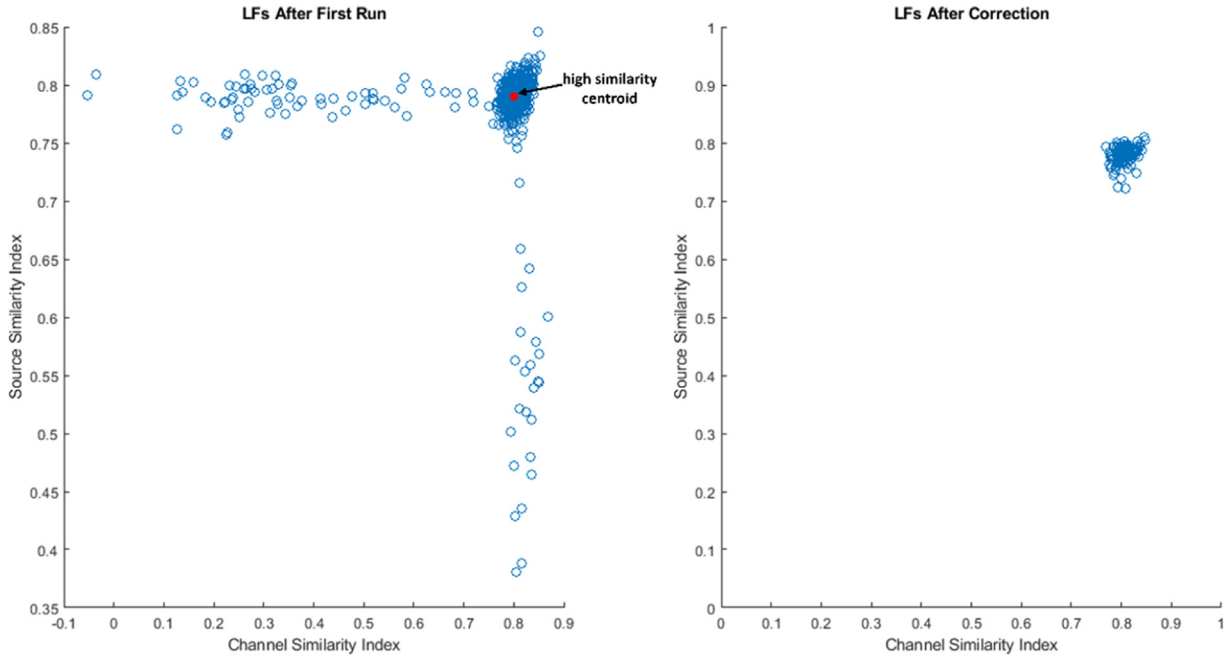

Fig. 17. Left: Scatter plot of the CSI and SSI for all 1251 LFs from the CMI dataset. Note that the cluster of LFs with high similarities has as its centroid (HSC) at (0.80,0.79). Right: Scatter plot of LFs that were corrected after screening with LF-AQI.

Table 2
IRT initial model result, factor loadings, and item discrimination for each question.

Questions	Factor loadings	Item discrimination
Q1	0.596	1.265
Q2	0.979	8.281
Q3	0.989	11.54
Q4	0.991	12.461
Q5	0.446	0.848
Q6	0.324	0.584

Table 3
Results for IRT model 2 with only the most relevant questions, factor loadings, and item discrimination for each question.

Questions	Factor loadings	Item discrimination
Q2	0.980	8.484
Q3	0.989	11.556
Q4	0.988	10.91

Table 4
model comparative indices.

Models	AIC	AICc	SABIC	BIC	Log Likely
Model 1: All Questions	9424.2	9425.5	9486.5	9581.8	−4682.08
Model 2: Q2, Q3, Q4	4523.0	4523.3	4554.2	4601.8	−2246.50

matic sensor correction during the head modeling step, we manually correct the electrode alignment and placement on the scalp. During the pipeline batch mode, the flagged files are post-processed by the module dedicated to Lead Field computation alone.

Once we have completed the corrections, we pass these LFs through the LF-AQI pipeline. Fig. 17 (left) shows the CSI and SSI scatter plot for the first run, showing that some lead fields have low correlations. Channel and Source similarity profiles for extreme cases of LFs with low correlations are shown in Fig. 18 (top row). The right side of Fig. 17 shows the scatter plot of CSI and SSI for the LFs after correction, and LF-AQI then accepted these LFs. Channel and Source similarity profiles for extreme cases after corrections are shown in Fig. 18 (bottom row).

3.7. Contrasting the lf-aqi with manual quality control

Once we had values for LF-AQI, we then performed manual quality control, and we compared the results to the LF-AQI results. We collected the manual quality control and LF-AQI results and performed the IRT analysis explained earlier.

The initial IRT model that we tested had all questions from the manual quality control questionnaire. Table 2 shows the results for that model. Each question has a label with a "Q" followed by a number from 1-to 6. Q2, Q3, and Q4 loaded very well on the latent factor with values > 0.9, whereas Q 6 has weak loading. The item discrimination scores were low for Q 5, Q6 ⟨ 1.0, whereas Q1 was marginal at 1.2. In contrast, Q2, Q3, and Q4 showed high discrimination values ⟩ 8.0.

The plots for the initial model are in Fig. 19. The x-axis is the latent variable θ, and the y-axis is the probability of theta$P(\theta)$, where P1 to P5 are the curves for each answer category. The plot shows the spread for each response category across different levels of θ. All response categories for Q3 and Q4 are a likely choice for some level of the latent variable θ. In contrast, Q1 has only the two most probable response categories. The overall model explained 60% variance.

Based on the initial model factor loadings, item discrimination scores, and trace plots, we have implemented another model with just Q2, Q3, and Q4 as these questions had high loadings, discrimination scores, and balanced trace plots. The results for the modified model are in Table 3. The factor loadings and item discrimination scores are slightly different from the initial model. However, the variance explained is 97%.

The results for the ANOVA between both models are in Table 4. The information Criterion shows that the second model is better, having low values (4523.0 & 4601.8) of AIC and BIC compared to the previous model's values (9424.2 & 9581.8). All the other model fit indices

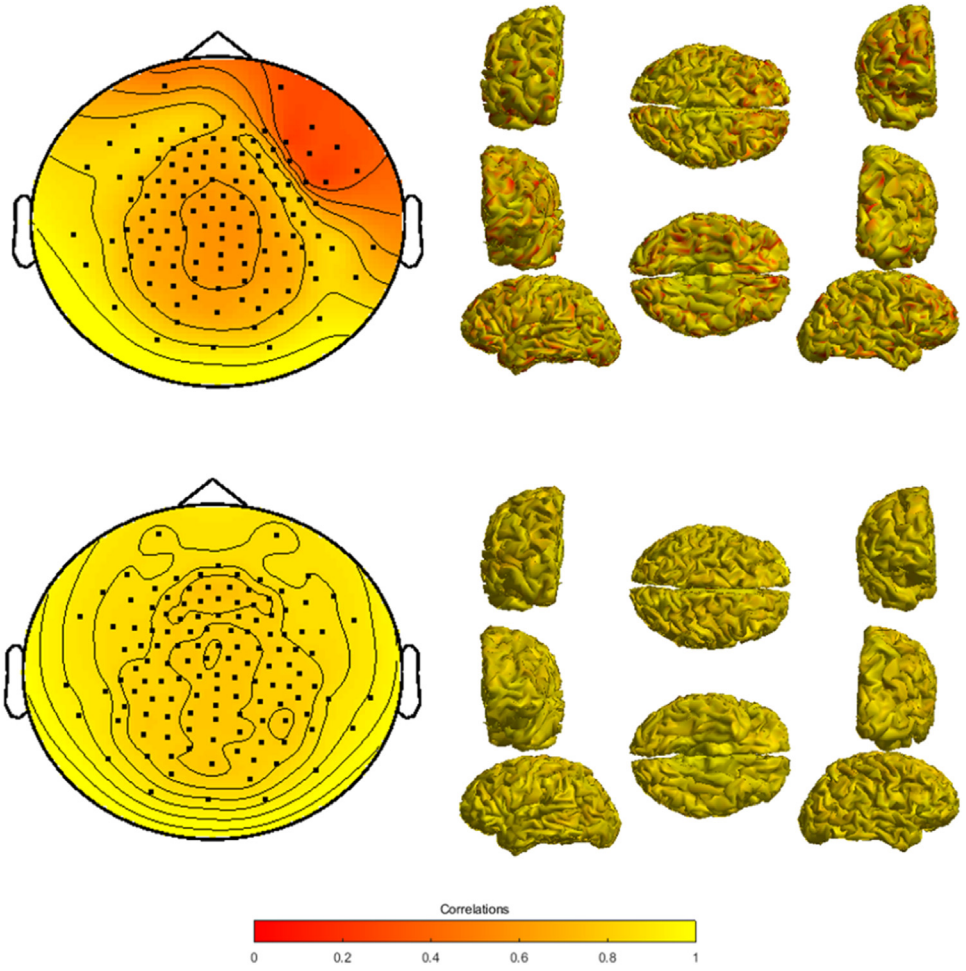

Fig. 18. First Row: Left - Similarity profile of subject having worst CSI. Right - Source Similarity Profile for a subject with the worst SSI, orange spots showing sources with low correlations. Second Row: Similarity profiles of both subjects after distance corrections.

Table 5
LMM fixed effect estimates with respective p-values and Cohen's d effect size.

LMM	Estimate	p-value	Cohen's d
$\vartheta_{channel} \sim \theta + random(Evaluator)$	0.15	<0.001	1.4
$\vartheta_{source} \sim \theta + random(Evaluator)$	0.00005	0.974	0.002
$\text{LF} - \text{AQI} \sim \theta + random(Evaluator)$	−0.098	<0.001	−1.3

greatly improved when we only applied IRT in Q2, Q3, and Q4. Thus, we selected the second model and generated the latent factor scores for further analysis.

After generating the latent factor scores from model 2 for each sample/subject, we compared these scores with the respective automated quality control scores for each CMI subject. A Fisher's z-transform scaled the automatic quality control values. Table 5 shows LMM models and the estimates for fixed effects with respective p-values and effect sizes. The latent factor theta is positively associated with CSI, resulting in a highly significant p-value (<0.001) and a large effect size (d = 1.4). LF-AQI has a similar trend with a negative association (p-value <0.001, d=−1.3). The LF-AQI values increase and deviate from the acceptable range as the quality of LF goes from good to unacceptable values; that is the reason for the negative association. In contrast, the association between manual quality control and SSI is not significant because, in manual quality control, we only analyzed LVF plots.

4. Discussion

Assessing the quality of 100 s and 1000s of lead fields (LFs) using conventional manual quality control methods is tedious and sometimes impractical. That is why there is a need to develop an automatic quality control method that checks the quality of LFs and declares them useable for source localization. In this study, an automatic lead field quality index (LF-AQI) is proposed to check for "doubtful" LFs form a bulk of EEG LFs. Channel and source similarity profiles (CSP, SSP) between simpler reference LF, homogeneous head model LF (HHM-LF), and realistic head models LFs, Boundary Element Method (BEM), and Finite Element Method (FEM) show high similarity profiles (correlations). These high values of the similarity profiles suggested that the HHM-LF can be used to detect numerical errors in realistic LFs.

To test this assumption, we conducted numerical simulations to assess the sensitivity of the CSP and SSP. We created a set of artifactual LFs by adding large values to the LF as the gold standard in this paper. These sensitivity checks revealed that similarity profiles are susceptible to any simulated artifacts. While the CSP and SSP help reveal the nature of the numerical problems encountered, they can be summarized by their minimum values, Channel and Source Similarity Indices, abbreviated as CSI and SSI, respectively.

Subsequently, we computed the CSI and SSI of 1251 LFs from MRIs obtained from the Child Mind Institute (CMI) dataset. We plotted the (CSI, SSI) points for all individuals on a 2D space. Most of the (CSI, SSI) points were clustered around a high similarity centroid (HSC), indicating the correspondence to the HHM-LF. However, there were out-

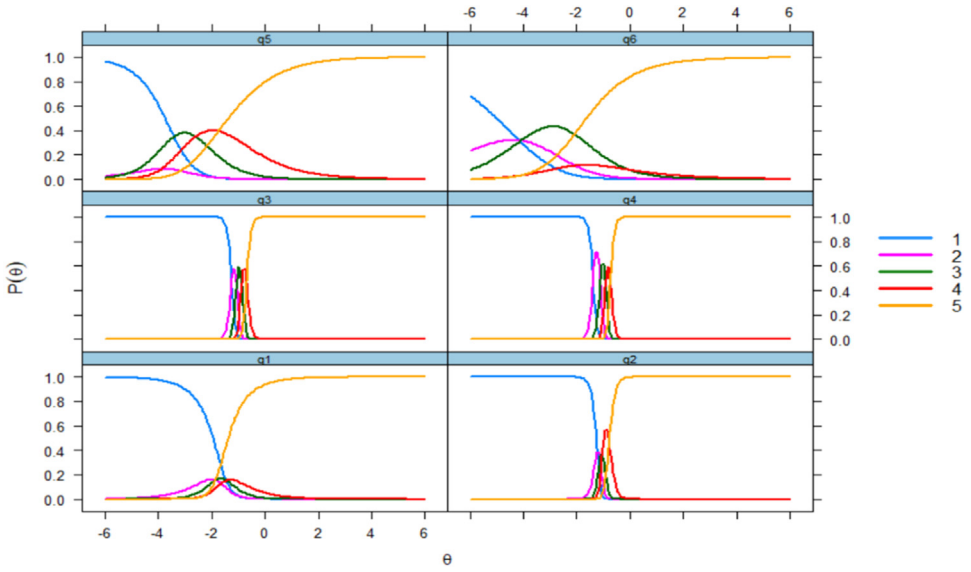

Fig. 19. Trace plots for each question. P1 to P5 is the answer scale. The X-axis is the value of the latent variable (θ), and the y-axis is the probability $P(\theta)$, which shows the chance of occurrence for each response category across different levels θ. Q3 and Q4 show a well-balanced trace plot where all answer categories are likely to answer at some level θ. Q2 and Q5 have four likely answer categories rather than five. In Contrast, Q1 has only two answer categories.

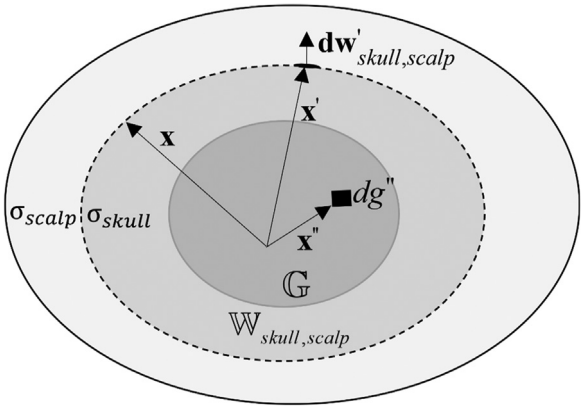

Fig. 20. Illustration of the volume conductor model and geometrical elements describing the electric potential $v(\mathbf{x})$ produced at any location $\mathbf{x}$ from volumetric primary current density currents $\boldsymbol{\iota}(\mathbf{x}'')$ distributed at locations $\mathbf{x}'' \in \mathbb{G}$. The medium is composed of volumes or compartments delimited by boundaries or closed surfaces $\mathbb{W}_{ij}$, modeled as piecewise homogeneous conductors with σ_{scalp} and σ_{skull} identifying these conductivities. A principle of superposition builds the potential $v(\mathbf{x})$ based on contributions from the region $\mathbb{G}$ of actual currents $\boldsymbol{\iota}(\mathbf{x}'')$and from the boundaries$\mathbb{G}_{ij}$ of virtual currents, which are proportional to the oriented surface elements $\mathbf{dw}'_{skull,scalp}$ at locations x'.

liers corresponding to LFs with a low value of either CSI or SSI. We defined our LF-AQI as the $\log_{10}$ of Euclidean distance between HSC and the (CSI, SSI) point for an LF as the LF-AQI for a given LF. We selected the 90th percentile of the LF-AQI for all 1251 LF-AQIs to find a threshold (−0.9755 for the CMI dataset). This threshold allowed us to identify the LFs with LF-AQI greater than this value as doubtful and needing revision. This categorization helped attain the goal of automatic quality checks of LFs since the LF-AQI did not exceed the threshold after the revision of the suspect LFs.

We note that the LF-AQI was tested for out-of-sample validity, which promises its effectiveness for new datasets. This feature helps use LF-AQI for datasets it was not trained before or for those recorded in different geographical conditions and age groups.

An interesting observation in our study is that for more accurately modeled LFs, even though modeling more tissue layers affect the eventual LF of a realistic and accurate head model, the dominating factor in calculating the eventual LF matrix remains the distances between sources and electrodes, and their orientation towards those electrodes. This conclusion results from the high correspondence between these realistic LF and the much simpler HHM-LF.

When a dipole is placed in an infinite homogenous medium, there will be a singularity when the distance between the electrode and the dipole approaches zero. This phenomenon seems to cause the “blow up” of LF values described in Section 2.1.1, for which we introduce the correction. In fact, in many publications (Drechsler, Wolters, Dierkes, Si, and Grasedyck, 2009; Piastra et al., 2018; Wolters, Köstler, Möller, Härdtlein, and Anwander, 2007) the voltage produced by the HHM-LF is known as the “singularity potential” v^{∞} (v^{hom} in our notation). For realistic LFs, the behavior of $v^{\infty}$is attenuated by a “correction potential,” which implies a correction to the LF. The expression of the correction potential for BEM is in section 10.4 of appendix Eq. (17). For FEM, this is most clearly seen when stating the difference method with calculating the LF (Eq. (18) of singularity paper). When working with either FEM or BEM LFs, we did not observe the “blow up” observed in the HHM-LF. We speculate that this “good” behavior of these realistic LFs may be due to the correction factors just mentioned. Of course, if by some mistake the head model erroneously places electrodes too near sources, this “blow up” might occur. To avoid the singularity, we introduce the correction in equations 4&5 to take advantage of the speed and simplicity of HHM-LF.

A practical outcome of this study is an LF-AQI pipeline, which applies the LF-AQI on a bulk set of LFs. This pipeline can work independently from subjective evaluations and indicate doubtful LFs already computed from other EEG LF pipelines. LF-AQI pipeline can also be embedded as a subpart of other pipelines and checks the quality of LFs on the go. This pipeline does not grade LFs from best to worst; instead, it flags them as accepted or doubtful. To our knowledge, this is the first and currently, only automatic quality control method that checks the quality of single or bulk LFs. Previously it was necessary to do this evaluation using manual, resource- and time-consuming techniques. As an illustration of the resource savings, we report that the automatic quality took less than 50 min of assessment time for 1251 LFs, while the manual quality assessment took 14 evaluators seven days.

We note that LF-AQI declared most LFs as acceptable and some as doubtful. When the LFs which were declared doubtful were investigated, three reasons for found for possible artifacts in the LFs: 1) blurred/noisy MRIs that can cause poor or inaccurate tissue segmentation, causing inaccurate tissue modeling, 2) incorrect alignment of cortex inside the head and 3) incorrect alignment of the electrodes. When these reasons were corrected, and newly computed LFs were assessed again using the

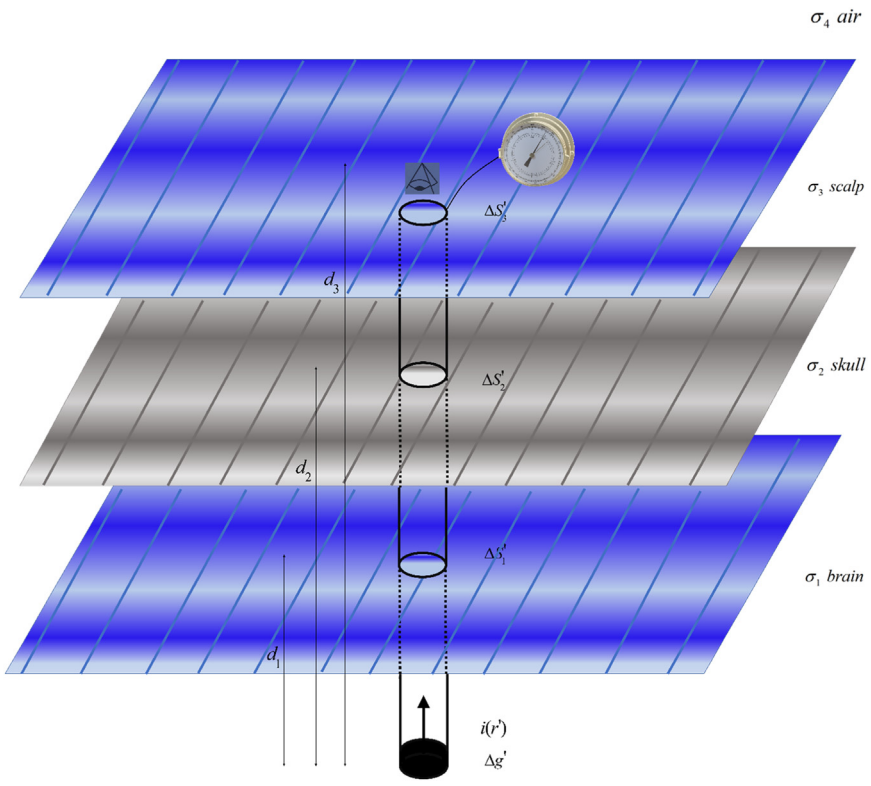

Fig. 21. A head model simulating a dipole under three planar conductors simulating the brain, skull, scalp, and air. We are recording the voltage on the scalp while assuming only the area inside the tube has conductivity, and the rest of it has zero conductivity.

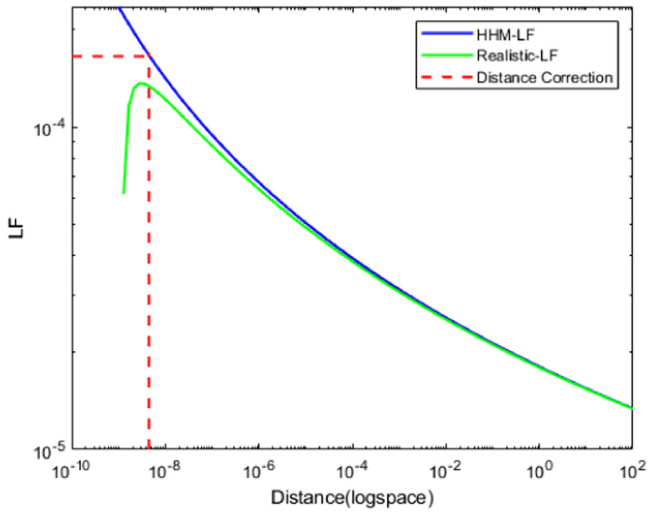

Fig. 22. A comparison of HHM-LF and Realistic LF values plotted against the distance(log-scaled) between the source and EEG sensor. As the distance decreases (for sources near the electrode), the value of realistic LF has dipped in their trend, which is not the case for the HHM-LF. The blowing up of these values is beyond a critical point, as the intersection of two red dotted lines.

LF-AQI pipeline, it labeled those LFs as accepted. This exercise shows that LF-AQI accurately detects the LFs with artifacts, and correcting the reasons for those assessments generates LF without any glaring problems and is more suitable for source localization. Like any other screening method, LF-AQI has false negatives and positives.

The equivalence of manual and automatic quality control was carefully controlled. Towards this end, the automatic LF-AQI check of the CMI database mentioned above was statistically compared to manual checking. We found that the quality of the LFs scored with the Likert scales via a structured instrument yielded latent factors highly correlated with our measure.

In this study, the LFs used to develop similarity profiles are highly accurate FEM-based LFs. However, the bulk LFs used in this study to test LF-AQI were BEM based. A future direction can be assessing bulk LFs computed using FEM, Finite Difference (FDM), and Finite Volume (FVM) based methods. This study would allow us to confirm the authority of LF-AQI for all currently used methods. Using LF-AQI to assess the quality of LFs generated for other imaging methods like MEG can be another future direction of this study. Lastly, developing quality check methods for other steps, i.e., MRI segmentation and realistic head modeling for tissues used for LF computation, can also be a future direction of this study.

Finally, we wish to emphasize that LF-AQI does NOT totally eliminate the need for human supervision of LF quality control. Instead, it helps focus on those LFs that might require supervision with the obvious savings in time. Moreover, the source spectra from the LFs passed by LF-AQI are being used in these studies (Riaz, 2021; Riaz et al., 2021; Riaz et al., 2021) with the LF passed through the LF-AQI pipeline.

5. Conclusion

This study proposes LF-AQI, an automated quality index for assessing the LFs computed from automated pipelines. Although these pipelines calculate LFs automatically, they eventually need human involvement to assess the quality of intermediate outputs and the LFs manually. This manual quality control becomes even more time-consuming and inefficient when working with a large dataset. We compute LF-AQI by comparing the test lead field with a homogenous lead field computed while considering the brain in an infinite and homogenous medium. LF-AQI was optimized using channel and source-wise correlation of complex, realistic, and gold standard LF first and then large dataset LFs from the CMI database. Later, we conducted a manual quality control exercise to validate LF-AQI results. The results from manual quality control and LF-AQI were highly associated. However, LF-AQI's time to measure the quality

was many folds less than the manual quality control. Thus, measuring the quality of LFs in large datasets using the LF-AQI is automated, quick, and reliable and will not have errors that might occur due to human intervention. The LF-AQI is working alongside an automatic pipeline for head modeling and source localization installed at joint CC-LAB, UESTC, China. The future extension of this study could be the development of automatic quality control indices for other intermediate steps involved in the computation of LFs. In addition, the LF-AQI could be extended for lead fields computed from other imaging modalities, i.e., Magnetoencephalography (MEG) and transcranial brain stimulation.

Funding

The authors used funding from the University of Electronic Sciences and Technology grant Y03111023901014005 and Chengdu Science and Technology Bureau Program under Grant 2022-GH02–00042-HZ to carry out this research.

CRediT author statement

Usama Riaz: Formal analysis, Software, Writing - original draft, Methodology **Fuleah A. Razzaq:** Formal analysis, Software, Writing - original draft **Ariosky Areces-Gonzalez:** Data curation **Deirel Paz-Linares:** Data curation and writing **Maria Carla Piastra:** Data curation and writing the manuscript. **Maria L. Bringas Vega:** Conceptualization, Supervision **Pedro A. Valdés-Sosa:** Conceptualization, Writing - review & editing, Supervision

Data availability

Code used in this study is openly available at

Lead field pipeline

https://github.com/CCC-members/HCP_compliant_processor
https://github.com/CCC-members/HCP_BST_source_head_modeler

LF-AQI

https://github.com/CCC-members/LF-AQI

Declaration of Competing Interest

The authors do not have any conflict of interest.

Acknowledgments

We would like to express our gratitude to **Eduardo Martinez Montes, José Enrique Alvarez Iglesias** from **Centro de Neurociencias de Cuba,** who contributed significantly to developing the LVF plots we used for manual quality assessment.

Appendix

Bayesian inverse approach and its dependence on LF

Electroencephalographic (EEG) Source Imaging is an imaging modality that uses the EEG to estimate the source, defined as the macroscopic primary current density $\mathbf{\iota}(\mathbf{x}_s, t)$, a 3-directional vector stochastic process in time t and at every gray matter location $\mathbf{x}_s$ (M. Hämäläinen, Hari, Ilmoniemi, Knuutila, and Lounasmaa, 1993; Riera and Fuentes, 1998). The stochastic process $\mathbf{\iota}(\mathbf{x}_s, t)$ originates primarily from the ensemble behavior (at a macroscopic scale of millimeters) of the postsynaptic potentials of geometrically aligned pyramidal cells in cortical columns (Freeman, 1975; Valdes-Sosa et al., 2009; Vinck and Perrenoud, 2019). Obtaining the sources $\mathbf{\iota}(\mathbf{x}_s, t)$ from the EEG is an inverse problem that requires a Forward Model:

$$\begin{aligned} &\mathbf{v}(\mathbf{x}_c, t) = \mathbf{k}(\mathbf{x}_c, \mathbf{x}_s)\mathbf{\iota}(\mathbf{x}_s, t) + \mathbf{\xi}(\mathbf{x}_c, t) \\ &or \\ &\mathbf{v}(t) = \mathbf{K}\,\mathbf{\iota} + \mathbf{\xi}(t) \end{aligned} \tag{14}$$

This equation specifies how sources are reflected in scalp voltage differences (M. S. Hämäläinen and Ilmoniemi, 1994). Forward models are summarized with a linear forward operator $\mathbf{k}(\mathbf{x}_c, \mathbf{x}_s)$ (Eq. (14)), a 3-dimensional column vector. The vector $\mathbf{k}(\mathbf{x}_c, \mathbf{x}_s)$ describes the relationship between the primary current density $\mathbf{\iota}(\mathbf{r}_g, t)$ and the measurements of electric potentials (EEG) or magnetic fields (MEG)$\mathbf{v}(\mathbf{x}_c, t)$at sensor locations $\mathbf{x}_c$. Where the forward operator $\mathbf{K}$ (in matrix notation), also denominated electric or magnetic Lead Field in neuroimaging (Baillet, Mosher, and Leahy, 2001), is a$N_c \times N_s$ or $N_c \times N_s \times 3$ matrix resulting from the forward model calculations over$N_c(\sim 10^2)$ sensor locations and over $N_s(\sim 10^4)$locations in a gray matter discretization. The notation $N_c \times N_s$ or $N_c \times N_s \times 3$ depends upon if the LF is in cartesian coordinates format or projected perpendicularly to the cortex plane t. $\mathbf{v}(t)$ and the sensor noise $\mathbf{\xi}(t)$ are both $N_c$dimensional vector stochastic processes while $\mathbf{\iota}(t)$ is a $3G$dimensional vector stochastic process.

Achieving precision in the inverse modeling of source activity $\mathbf{\iota}(\mathbf{x}_s, t)$, is an important issue (He et al., 2019; Reid et al., 2019), and it depends critically on the accuracy of the forward model (Akalin Acar and Makeig, 2013). Instability, multivariate, and nonlinear effect of the forward model on even the simplest inverse model, have been abundantly illustrated in the literature (Brookes et al., 2007; Friston et al., 2008; Grave De Peralta Menendez, Murray, Michel, Martuzzi, and Gonzalez Andino, 2004; Hauk, 2004; Mattout, Phillips, Penny, Rugg, and Friston, 2006; Michel et al., 2004; R.D. Pascual-Marqui, Michel, and Lehmann, 1994; Roberto D Pascual-Marqui et al., 2006; Paz-Linares et al., 2023; D. Paz-Linares et al., 2017; Trujillo-Barreto, Aubert-Vázquez, and Valdés-Sosa, 2004; Van Veen, Van Drongelen, Yuchtman, and Suzuki, 1997; D. Wipf and Nagarajan, 2009; D. P. Wipf, Ramırez, Palmer, Makeig, and Rao, 2006).

Inverse model

We illustrate the relation between lead field and inverse solutions by describing the Maximum Posterior Bayes (MAPB) estimators based on Gaussian probability distributions, though the arguments apply to any other family of inverse solutions.

Gaussian MAPB yield linear inverse operator (pseudo-inverse) $\mathbf{K}^+$, used to provide the estimate $\hat{\mathbf{\iota}}(t)$ of the theoretical $\mathbf{\iota}(t)$ (Grave de Peralta Menendez, Hauk, Gonzalez Andino, Vogt, and Michel, 1997; Grave De Peralta Menendez et al., 2004; Grech et al., 2008), detailed as follows:

$$\hat{\mathbf{\iota}}(t) = \mathbf{K}^+\left(\mathbf{K}, \mathbf{\Sigma}_{\xi\xi}, \mathbf{\Sigma}_u\right) v(t) \tag{15}$$

with $\mathbf{K}^+(\mathbf{K}, \mathbf{\Sigma}_{\xi\xi}, \mathbf{\Sigma}_u) = (\mathbf{K}^{\mathrm{T}}\mathbf{\Sigma}_{\xi\xi}^{-1}\mathbf{K} + \mathbf{\Sigma}_u^{-1})^{-1}\mathbf{K}^{\mathrm{T}}\mathbf{\Sigma}_{\xi\xi}^{-1}$where $\mathbf{K}^+$ represents a family of linear inverse solutions, requiring specification of the electric or magnetic Lead-Fields in $\mathbf{K}$, and also the specifications of $\mathbf{\Sigma}_{\xi\xi}$the covariance of the noise, and$\mathbf{\Sigma}_u$ the covariance of the source activity (Baillet and Garnero, 1997; D. Wipf and Nagarajan, 2009). This formation explicitly shows the possible propagation of errors due to the misspecification of the LF Matrix. It is obvious that errors resulting from calculations of the Lead-Field $\mathbf{K}$ in Eq. (14) would propagate in a multivariate and nonlinear fashion to an inverse solution $\hat{\mathbf{\iota}}(t)$ in Eq. (15).

Precise modeling (inverse or forward) should depend even more critically on the Lead-Field $\mathbf{K}$ obtained for highly detailed anisotropic 3D models of the geometry and electromagnetic properties of biological tissue (head) and each human individual (valid also for other animals) (Dannhauer et al., 2012; M. 2011; Hallez et al., 2007; Nolte and Dassios, 2005; Piastra et al., 2020; Vorwerk et al., n.d., 2014; Vorwerk, Oostenveld, Piastra, Magyari, and Wolters, 2018b; Windhoff et al., 2013; Yamaguchi, 2014). Such a level of detail is also accompanied by an increased computational cost and employing the Finite Element Method

(FEM) computations (Strang, Fix, and Griffin, 1974). Nevertheless, it is common in neuroimaging to assume isotropic and piecewise homogeneous electromagnetic properties of biological tissue to lighten computations and yet preserve a moderate level of detail in Lead-Field computations.

Even moderately detailed forward modeling must deal with the electric field potentials with conductivity heterogeneities at tissue boundaries (M. Hämäläinen et al., 1993; Riera and Fuentes, 1998) which leads to complex numerical computations via the Finite Element Method (FEM) (Dannhauer et al., 2012; M. 2011; Hallez et al., 2007; Nolte and Dassios, 2005; Piastra et al., 2020; Vorwerk et al., 2014, 2018a; Windhoff et al., 2013; Yamaguchi, 2014). or alternatively Boundary Elements Method (BEM) (Cheng and Cheng, 2005).

Piece-wise conductor forward model

Some forward modeling assumes a piecewise volume conductor BEM-based model (Fig. 20). Such models have divided the volume conductor into pieces with isotropic and homogeneous conductivities. These have passive nonmagnetic properties of the biological tissue and broadband stationarity of the electric potentials (Azizollahi, Aarabi, and Wallois, 2016; M. Dannhauer et al., 2011; Jochmann, Güllmar, Haueisen, and Reichenbach, 2011; Lanfer et al., 2012; Turovets, Poolman, Salman, Malony, and Tucker, 2008; Vorwerk et al., 2019, n.d.). Under such assumptions, this stationary potential $v(\mathbf{x})$at any location$\mathbf{x}$and without regard for the time$t$is described by a linear integral Eq. (16) as a consequence of Maxwell equations (Geselowitz, 1967; Vladimirov, 1976).

$$\frac{\sigma_{skull}+\sigma_{scalp}}{2\sigma_o}v(\mathbf{x}) = \underbrace{v^{\hom}(\mathbf{x})}_{\text{singularitypotential}} + \underbrace{\frac{1}{4\pi\sigma_{brain}}\sum_{skull,scalp}\left(\sigma_{skull}-\sigma_{scalp}\right)\oiint_{\mathbb{W}_{skull,scalp}} v(\mathbf{x}')\frac{(\mathbf{x}-\mathbf{x}')\cdot\mathbf{dw}'_{skull,scalp}}{|\mathbf{x}-\mathbf{x}'|^3}}_{\text{CorrectionPotential}} \quad (16)$$

with $v^{\hom}(\mathbf{x}) = \frac{1}{4\pi\sigma_{brain}}\odot\!\!\int_{\mathbb{C}} \boldsymbol{\iota}(\mathbf{x}'')\cdot\frac{(\mathbf{x}-\mathbf{x}'')}{|\mathbf{x}-\mathbf{x}'|^3}dc''$

Here, the subscripts *brain, skull,* and *scalp* represent the conductivity of the tissues of isotropic and homogeneous compartments. $\sigma_{skull}$and σ_{scalp} are conductivities of contiguous compartments in the piecewise conductor medium (Fig. 3), $\sigma_{brain}$is the air brain permittivity (≈ 1), $v^{\hom}(\mathbf{x})$is the electric potential produced by a volumetric primary current density $\boldsymbol{\iota}(\mathbf{x}'')$ at source locations $\mathbf{x}''$and assuming no boundaries homogeneous electric permittivity σ_{brain}, the second term in equation explains virtual surface current densities due to conductivity heterogeneities $(\sigma_{skull}-\sigma_{scalp})$ at boundary locations $\mathbf{x}'$.

An electric (EEG) Lead-Field $\mathbf{k}(x_c,x_s)$depends on the solution for Eq. (16), assuming an elementary current or Dirac delta function $\boldsymbol{\iota}(x'') = \mathbf{d}\delta(x''-x_s)$ at each source location $x''=x_s$, each EEG electrode location $x=x_c$, and each cartesian direction$\mathbf{d}=\mathbf{d}_1,\mathbf{d}_2,\mathbf{d}_3$. So, if we write Eq. (16) as an equation computing element of an LF matrix for the type of head model shown in Fig. 20, it can be written as:

$$k_{c,s} = \frac{1}{4\pi\sigma_{brain}}\left(\frac{\mathbf{x}-\mathbf{x}_{c,s}\cdot\boldsymbol{\mu}_s}{|\mathbf{x}-\mathbf{x}'|^3}\right) + \frac{1}{4\pi\sigma_{brain}}\sum_{skull,scalp}\left(\sigma_{skull}-\sigma_{scalp}\right)\oiint_{\mathbb{W}_{skull,scalp}} v(\mathbf{x}')\frac{(\mathbf{x}-\mathbf{x}')\cdot\mathbf{dw}'_{skull,scalp}}{|\mathbf{x}-\mathbf{x}'|^3} \quad (17)$$

Here, the subscripts *brain, skull,* and *scalp* represent the conductivity of the tissues of isotropic and homogeneous compartments shown in Fig. 20.

An estimated solution to the core problem of determining the electric Lead-Fields $\mathbf{k}(x_c,x_s)$, or electric potential in Eq. (16), is then via BEM computations (Akalin Acar and Makeig, 2013; Ermer et al., 2001; Fuchs et al., 2002; Huang et al., 1999; Mosher et al., 1993, 1999; Opitz et al., 2018; Rahmouni et al., 2019; Vatta et al., 2010).

The EEG Lead-Fields $\mathbf{K}$ instead reflect directly such conductivity heterogeneities (Eq. (16)), which are also evidenced directly in EEG measurements $v(t)$ (M. Dannhauer et al., 2011; De Munck, Wolters, and Clerc, 2012; Ermer et al., 2001; Lanfer et al., 2012; Mosher et al., 1993, 1999; Vorwerk et al., n.d.).

A differential Piece-wise conductor forward model

In this section, we explain the reason for the distance correction made in Section 2.1.1 for HHM-LF when the sources are too close to a specific EEG sensor. To explain the reason for this correction, we propose an approximation of the Boundary Element Method (BEM) head model, as shown in Fig. 21. In this figure, we assume we are observing and recording the surface voltage on a planar head model only through a cylindrical pipe across all tissue layers of the piecewise volume conductor model. This model is designed so that the voltage recorded at the scalp (mentioned using a circle) is only affected by the conductivity effect of intermediate layers (also shown in circles).

These cylindrical tissues represent 3 compartments brain, skull, and scalp. The conductivities of each compartment are, $\sigma_1 = 0.3300$, $\sigma_2 = 0.0042$ and$\sigma_3 = 0.3300$ respectively, and the air conductivity is set at $\sigma_4 = 0$. The skull and scalp tissues are between the brain and air conductivities. However, the brain extends to $-\infty$, and the air extends to $+\infty$, making both semi-bounded. While performing this BEM computations, we assumed a scenario in which an insulating medium covers the walls of the cylindrical pipe from which we are observing. This assumption rules out the effect of surroundings inside the cylindrical volume we defined earlier. We also assumed the thickness of the skull and tissue layers was equal to 0.005 m.

We consider current dipoles across the section, distributed in a disk-like geometry with differential volume elementsΔg oriented in the$z$-axis direction ($\mathbf{e}_z$). Within the cortical section and for each differential element of volume (Δg) a projected to normal oriented field defines the primary current density ($\boldsymbol{\iota} = \mu\mathbf{e}_z$) and the dipolar moment $\boldsymbol{\mu} = \mu\Delta g\mathbf{e}_z$.

The general BEM equation (Eq. (16)) then reduces to a finite difference Eq. (18) for the electric potential at a given tissue boundary v_i. First, the current dipole, as shown in Eq. (19), contributes to this potential, which causes the homogeneous potential $v_i^{\hom}$ to be inversely proportional to the square distance d_i^2. Second, virtual currents at the remaining boundaries are caused by the potentials v_j and are inversely proportional to the square distances d_{ij}^2. The contributions of the virtual currents are weighted positively or negatively depending on whether thej^{th} boundary lies below or above the i^{th} boundary. This phenomenon causes the scalar product in (Eq. (15)) to be positive or negative depends on the$sign(i-j)$.

$$\frac{(\sigma_i+\sigma_{i+1})}{2\sigma_o}v_i = v_i^{\hom} - \frac{1}{4\pi\sigma_o}\sum_{j\neq i}(\sigma_j-\sigma_{j+1})v_j\Delta S\frac{sign(i-j)}{d_{ij}^2} \quad (18)$$

$$v_i^{\hom} = \frac{1}{4\pi\sigma_o}\frac{\mu\Delta g}{d_i^2} \quad (19)$$

The finite difference Eq. (18) could be redefined in matrix form into Eq. (20).

$$\Sigma v = v^{\hom} or v = \Sigma^{-1}v^{\hom} \quad (20)$$

Here v and $v^{\hom}$ are the vectors whose entries comprise the realistic and homogeneous electric potential at the boundaries, respectively, as shown in Eqs. (21) and 22. TheΣ in Eq. (20) is the head model matrix shown in Eq. (23), whose entries comprise the distances and conductivities.

$$v = \left(v_1 \ldots v_i \ldots v_n\right)^T \quad (21)$$

$$v = \left(v_1^{\hom} \ldots v_i^{\hom} \ldots v_n^{\hom}\right)^T \quad (22)$$

$$\Sigma = \begin{pmatrix} \Sigma_{11} & & & & & & \\ & \ddots & & & & & \\ & & \Sigma_{ii} & \cdots & \Sigma_{ij} & & \Sigma_{in} \\ & & & \ddots & & & \\ & & \Sigma_{ji} & \cdots & \Sigma_{jj} & \cdots & \Sigma_{jn} \\ & & \vdots & & \vdots & \ddots & \vdots \\ & & \Sigma_{ni} & \cdots & \Sigma_{nj} & \cdots & \Sigma_{nn} \end{pmatrix} \quad (23)$$

Here $\Sigma_{ii} = \frac{\sigma_i + \sigma_{i+1}}{2\sigma_o}$ and $\Sigma_{ij} = \frac{1}{4\pi\sigma_o}(\sigma_j - \sigma_{j+1})\Delta S \frac{sign(i-j)}{d_{ij}^2}$.

The results of BEM calculations due to this matrix are shown in (Fig. 22). This figure shows the outcome of the HHM-LF with a critical point showing where correction is needed. The figure also shows the corresponding realistic LF values for which the HHM-LF is obtained. This realistic LF is derived from the electric potentials measured by the sensor placed at the air/scalp boundary, as shown in the figure (Fig. 22). LF values are plotted as the dependent variable, and a log-scaled distance is an independent variable. The result shows that HHM-LF and their corresponding realistic LF start diverging at the same point as the distance between the sources and the EEG sensor decreases. Eventually, at a critical point, the realistic LF faces a dip in the LF values in contrast to the HHM-LF, whose values blow up below this critical point. The sources whose distance is below this critical point (intersection of two dotted red lines) are where we apply the distance correction. The value of the critical point in terms of regular scale is around a distance of 0.007 m. The reason for the divergence between the curves of LFs comes from the explanation in discussion. The curve in green color is derived from the Eqs. (17),18, and 19. In this study, we apply corrections at a critical point which we call earlier distance correction.

References

Adjerid, S., & Weinhart, T. (2011). *Linear symmetrizable hyperbolic systems*. 80(275), 1335–1367.

Akalin Acar, Z., Makeig, S, 2013. Effects of forward model errors on EEG source localization. Brain Topogr. 26 (3), 378–396. doi:10.1007/s10548-012-0274-6.

Alexander, L.M., Escalera, J., Ai, L., Andreotti, C., Febre, K., Mangone, A., … Milham, M.P., 2017. Data Descriptor: an open resource for transdiagnostic research in pediatric mental health and learning disorders. Sci. Data 4. doi:10.1038/sdata.2017.181.

Anderson-Cook, C.M., 2007. Generalized additive models: an introduction with R. J. Am. Stat. Assoc. 102 (478), 760–761. doi:10.1198/jasa.2007.s188.

Areces-Gonzalez, A., 2020. MRI-DWI-MEEG pipeline for individualized insilico BigBrain like preparation. *Organ. Hum. Brain Mapping, Canada,* Abstract 1548.

Azizollahi, H., Aarabi, A., Wallois, F., 2016. Effects of uncertainty in head tissue conductivity and complexity on EEG forward modeling in neonates. Hum. Brain Mapp. 37 (10), 3604–3622.

Baillet, S., Garnero, L., 1997. A Bayesian approach to introducing anatomo-functional priors in the EEG/MEG inverse problem. IEEE Trans. Biomed. Eng. 44 (5), 374–385. doi:10.1109/10.568913.

Baillet, S., Mosher, J.C., Leahy, R.M., 2001. Electromagnetic brain mapping. IEEE Signal Process Mag. 18 (6), 14–30. doi:10.1109/79.962275.

Beaujean, A.A., 2014. Latent variable modeling using R: a step-by-step guide. Latent Variable Modeling Using R: A Step-by-Step Guide doi:10.4324/9781315869780.

Bird, R.E., Coombs, W.M., Giani, S., 2019. A posteriori discontinuous Galerkin error estimator for linear elasticity. Appl. Math. Comput. 344–345, 78–96. doi:10.1016/j.amc.2018.08.039.

Brookes, M.J., Stevenson, C.M., Barnes, G.R., Hillebrand, A., Simpson, M.I.G., Francis, S.T., Morris, P.G., 2007. Beamformer reconstruction of correlated sources using a modified source model. Neuroimage 34 (4), 1454–1465. doi:10.1016/j.neuroimage.2006.11.012.

Chalmers, R.P., 2012. mirt: a Multidimensional Item Response Theory Package for the R Environment. JSS J. Statist. Software 48. Retrieved from http://www.jstatsoft.org/ .

Chalmers, P. (2015). *Item response theory Unidimensional IRT Multidimensional IRT Diagnostics Estimation Package Specifics Multiple Group IRT, DIF, and DTF Multidimensional Item Response Theory Workshop in R.*

Chalmers, R.P., 2015b. Extended Mixed-Effects Item Response Models With the MH-RM Algorithm. J. Educ. Meas 52 (2), 200–222. doi:10.1111/jedm.12072.

Cheng, A.H.-D., Cheng, D.T, 2005. Heritage and early history of the boundary element method. Eng. Anal Bound Elem 29 (3), 268–302.

Clarke, L.P., Camacho, M.A., Heine, J.J., Vaidyanathan, M., Hall, L.O., Thatcher, R.W., … Velthuizen, R.P., 1995. MRI segmentation: methods and applications. Magn. Reson. Imaging 13 (3), 343–368.

Cook, M.J.D., Koles, Z.J., 2006. A high-resolution anisotropic finite-volume head model for EEG source analysis. In: Annual International Conference of the IEEE Engineering in Medicine and Biology - Proceedings, pp. 4536–4539. doi:10.1109/IEMBS.2006.260314.

Cuartas Morales, E., Acosta-Medina, C.D., Castellanos-Dominguez, G., Mantini, D, 2019. A finite-difference solution for the eeg forward problem in inhomogeneous anisotropic media. Brain Topogr. 32 (2), 229–239. doi:10.1007/s10548-018-0683-2.

Dannhauer, M., Lanfer, B., Wolters, C.H., Knösche, T.R., 2011. Modeling of the human skull in EEG source analysis. Hum. Brain Mapp. 32 (9), 1383–1399. doi:10.1002/hbm.21114.

Dannhauer, M., Brooks, D., Tucker, D., MacLeod, R., 2012. A pipeline for the simulation of transcranial direct current stimulation for realistic human head models using SCIRun/BioMesh3D. In: Proceedings of the Annual International Conference of the IEEE Engineering in Medicine and Biology Society, EMBS, pp. 5486–5489. doi:10.1109/EMBC.2012.6347236.

De Munck, J.C., Wolters, C.H., Clerc, M., 2012. EEG and MEG: forward modeling. Handbook of Neural Activity Measure. 19, 192–248.

Delorme, A., Makeig, S., 2004. EEGLAB: an open source toolbox for analysis of single-trial EEG dynamics including independent component analysis. J. Neurosci. Methods 134 (1), 9–21. doi:10.1016/j.jneumeth.2003.10.009.

Despotović, I., Goossens, B., Philips, W., 2015. MRI segmentation of the human brain: challenges, methods, and applications. Comput. Math. Methods Med. 2015. doi:10.1155/2015/450341.

Dickie, E.W., Anticevic, A., Smith, D.E., Coalson, T.S., Manogaran, M., Calarco, N., … Voineskos, A.N., 2018. Ciftify: a framework for surface-based analysis of legacy MR acquisitions. Biorxiv doi:10.1101/484428.

Drechsler, F., Wolters, C.H., Dierkes, T., Si, H., Grasedyck, L., 2009. A full subtraction approach for finite element method based source analysis using constrained Delaunay tetrahedralisation. Neuroimage 46 (4), 1055–1065. doi:10.1016/j.neuroimage.2009.02.024.

Ermer, J.J., Mosher, J.C., Baillet, S., Leahy, R.M., 2001. Rapidly recomputable EEG forward models for realistic head shapes. Phys. Med. Biol. 46 (4), 1265–1281. doi:10.1088/0031-9155/46/4/324.

Fischl, B., 2012. FreeSurfer. Neuroimage 62, 774–781. doi:10.1016/j.neuroimage.2012.01.021.

Fox, J. (2015). *Applied regression analysis and generalized linear models.*

Freeman, W.J., 1975. Mass Action in the Nervous system : Examination of the Neurophysiological Basis of Adaptive Behavior Through the EEG. Academic Press, New York ; London.

Friston, K., Harrison, L., Daunizeau, J., Kiebel, S., Phillips, C., Trujillo-Barreto, N., … Mattout, J., 2008. Multiple sparse priors for the M/EEG inverse problem. Neuroimage 39 (3), 1104–1120. doi:10.1016/j.neuroimage.2007.09.048.

Fuchs, M., Kastner, J., Wagner, M., Hawes, S., Ebersole, J.S., 2002. A standardized boundary element method volume conductor model. Clin. Neurophysiol. 113 (5), 702–712. doi:10.1016/S1388-2457(02)00030-5.

Geffroy, D., Rivière, D., Denghien, I., Souedet, N., Laguitton, S., Cointepas, Y., 2011. BrainVISA : a complete software platform for neuroimaging. Python in Neurosci. Workshop.

Geselowitz, D.B., 1967. On bioelectric potentials in an inhomogeneous volume conductor. Biophys. J. 7 (1), 1–11.

Glasser, M.F., Sotiropoulos, S.N., Wilson, J.A., Coalson, T.S., Fischl, B., Andersson, J.L., … Jenkinson, M., 2013. The minimal preprocessing pipelines for the human connectome project. Neuroimage 80, 105–124. doi:10.1016/j.neuroimage.2013.04.127.

Gonzalez, A., & Michael, Y. (2023). *Multimodal pipeline for HCP-compatible processing and registration of legacy datasets (MRI, MEG, and EEG)*. https://doi.org/10.36227/techrxiv.22276549.v1

Gramfort, A., Papadopoulo, T., Olivi, E., Clerc, M., 2010. OpenMEEG: opensource software for quasistatic bioelectromagnetics. Biomed. Eng. Online 9 (1), 45. doi:10.1186/1475-925X-9-45.

Gramfort, A., Papadopoulo, T., Olivi, E., Clerc, M., 2011. Forward field computation with OpenMEEG. Comput. Intell. Neurosci. 2011. doi:10.1155/2011/923703.

Gramfort, A., Luessi, M., Larson, E., Engemann, D.A., Strohmeier, D., Brodbeck, C., … Hämäläinen, M.S., 2014. MNE software for processing MEG and EEG data. Neuroimage 86, 446–460. doi:10.1016/j.neuroimage.2013.10.027.

Grant, P.F., Lowery, M.M., 2009. Electric field distribution in a finite-volume head model of deep brain stimulation. Med. Eng. Phys. 31 (9), 1095–1103. doi:10.1016/j.medengphy.2009.07.006.

Grave de Peralta Menendez, R., Hauk, O., Gonzalez Andino, S., Vogt, H., Michel, C., 1997. Linear inverse solutions with optimal resolution kernels applied to electromagnetic tomography. Hum. Brain Mapp. 5 (6), 454–467.

Grave De Peralta Menendez, R., Murray, M.M., Michel, C.M., Martuzzi, R., Gonzalez Andino, S.L., 2004. Electrical neuroimaging based on biophysical constraints. Neuroimage 21 (2), 527–539. doi:10.1016/j.neuroimage.2003.09.051.

Grech, R., Cassar, T., Muscat, J., Camilleri, K.P., Fabri, S.G., Zervakis, M., … Vanrumste, B., 2008. Review on solving the inverse problem in EEG source analysis. J. Neuroeng. Rehabil. 5. doi:10.1186/1743-0003-5-25.

Hämäläinen, M.S., Ilmoniemi, R.J., 1994. Interpreting magnetic fields of the brain: minimum norm estimates. Med. Biol. Eng. Comput. 32 (1), 35–42. doi:10.1007/BF02512476.

Hämäläinen, M., Hari, R., Ilmoniemi, R.J., Knuutila, J., Lounasmaa, O.V., 1993. Magnetoencephalography—Theory, instrumentation, and applications to noninvasive studies of the working human brain. Rev. Mod. Phys. 65 (2), 413.

Hallez, H., Vanrumste, B., Grech, R., Muscat, J., De Clercq, W., Vergult, A., … Lemahieu, I., 2007. Review on solving the forward problem in EEG source analysis. J. Neuroeng. Rehabil. 4. doi:10.1186/1743-0003-4-46.

Hand, D.J. (.1987). *Multivariate analysis of variance and repeated measures; a practical approach for behavioural scientists.*

Hauk, O., 2004. Keep it simple: a case for using classical minimum norm estimation in the analysis of EEG and MEG data. Neuroimage 21 (4), 1612–1621. doi:10.1016/j.neuroimage.2003.12.018.

He, B., Astolfi, L., Valdes-Sosa, P.A., Marinazzo, D., Palva, S.O., Benar, C.G., … Koenig, T.,

2019. Electrophysiological Brain Connectivity: theory and Implementation. IEEE Trans. Biomed. Eng. 66 (7), 2115–2137. doi:10.1109/TBME.2019.2913928.
Heckemann, R.A., Hajnal, J.V., Aljabar, P., Rueckert, D., Hammers, A., 2006. Automatic anatomical brain MRI segmentation combining label propagation and decision fusion. Neuroimage 33 (1), 115–126. doi:10.1016/j.neuroimage.2006.05.061.
Helmholtz, H., 1876. Heidelberger Texte zur Mathematikgeschichte the origin and meaning of geometrical axioms i. the origin and meaning of geometrical axioms. Source: Mind 1 (3), 301–321.
Howell, D.C., 2014. Median Absolute Deviation. Wiley StatsRef: Stat. Reference Online 3, 0–1. doi:10.1002/9781118445112.stat06232.
Hu, S., Yao, D., Bringas-Vega, M.L., Qin, Y., Valdes-Sosa, P.A., 2019. The Statistics of EEG Unipolar References: derivations and Properties. Brain Topogr. 32 (4), 696–703. doi:10.1007/s10548-019-00706-y.
Huang, M.X., Mosher, J.C., Leahy, R.M., 1999. A sensor-weighted overlapping-sphere head model and exhaustive head model comparison for MEG. Phys. Med. Biol. 44.
IBSR. (2013). "The Internet Brain Segmentation Repository,."
Jas, M., Larson, E., Engemann, D.A., Leppäkangas, J., Taulu, S., Hämäläinen, M., Gramfort, A., 2018. A reproducible MEG/EEG group study with the MNE software: recommendations, quality assessments, and good practices. Front. Neurosci. (AUG) 12. doi:10.3389/fnins.2018.00530.
Jenkinson, M., Beckmann, C.F., Behrens, T.E.J., Woolrich, M.W., Smith, S.M., 2012. FSL. Neuroimage 62 (2), 782–790. doi:10.1016/j.neuroimage.2011.09.015.
Jochmann, T., Güllmar, D., Haueisen, J., Reichenbach, J.R., 2011. Influence of tissue conductivity changes on the EEG signal in the human brain–A simulation study. Zeitschrift Für Medizinische Physik 21 (2), 102–112.
Kleiman, E. (2021). *Package 'EMAtools.'*
Kn, T.R., Haueisen, J., 2022. EEG /MEG Source Reconstruction. Springer.
Lanfer, B., Scherg, M., Dannhauer, M., Knösche, T.R., Burger, M., Wolters, C.H., 2012. Influences of skull segmentation inaccuracies on EEG source analysis. Neuroimage 62 (1), 418–431. doi:10.1016/j.neuroimage.2012.05.006.
Linear, T., Mixed, N., Models, E., Fit, D., & Hmisc, S. (2022). *Package 'nlme.'*
Malmivuo, J. (1995). *Bioelectromagnetism - Principles and Applications of Bioelectric and Biomagnetic Fields*. https://doi.org/10.1093/acprof:oso/9780195058239.001.0001
Malmivuo, J., 2000. Biomagnetism. CRC Press LLC.
Mattout, J., Phillips, C., Penny, W.D., Rugg, M.D., Friston, K.J., 2006. MEG source localization under multiple constraints: an extended Bayesian framework. Neuroimage 30 (3), 753–767.
Medani, T., Garcia-Prieto, J., Tadel, F., Schrader, S., Antonakakis, M., Joshi, A.A., …. Leahy, R.M. (.2021a). Realistic head modeling of electromagnetic brain activity: an integrated Brainstorm-DUNEuro pipeline from MRI data to the FEM solutions. 135. https://doi.org/10.1117/12.2580935
Medani, T., Garcia-Prieto, J., Tadel, F., Schrader, S., Antonakakis, M., Joshi, A.A., …. Leahy, R.M. (.2021b). *Realistic head modeling of electromagnetic brain activity: an integrated Brainstorm-DUNEuro pipeline from MRI data to the FEM solutions*. 1159554(February), 135. https://doi.org/10.1117/12.2580935
Michel, C.M., Murray, M.M., Lantz, G., Gonzalez, S., Spinelli, L., Grave De Peralta, R., 2004. EEG source imaging. Clin. Neurophysiol. 115 (10), 2195–2222. doi:10.1016/j.clinph.2004.06.001.
Mosher, J.C., Leahy, R.M., Lewis, P.S., 1993. Matrix Kernels for the Forward Problem in EEG and MEG. Energy 14, 1–9.
Mosher, J.C., Leahy, R.M., Lewis, P.S., 1999. EEG and MEG: forward solutions for inverse methods. IEEE TRANS. BIOMED. ENG. 46.
Mosher, J.C., .Baillet, S., Darvas, F., Pantazis, D., Kucukaltun-Yildirim, E., & Leahy, R.M. (.n.d.). *BrainStorm Electromag. Imaging Software*. Retrieved from http://neuroimage.usc.edu/brainstorm.
Nolte, G., Dassios, G., 2005. Analytic expansion of the EEG lead field for realistic volume conductors. Phys. Med. Biol. 50 (16), 3807–3823. doi:10.1088/0031-9155/50/16/010.
Nunez, P.L., Srinivasan, R., 2006a. Electric Fields of the brain: the Neurophysics of EEG. Oxford University Press, USA.
Nunez, P.L., Srinivasan, R., 2006b. Electric Fields of the Brain: The neurophysics of EEG, 2nd ed. doi:10.1093/acprof:oso/9780195050387.001.0001.
O'Brien, R.G., Kaiser, M.K., 1985. MANOVA for analyzing repeated measurement design: an extensive primer. Psychol. Bull. 92 (2), 316–333.
Oostenveld, R., Fries, P., Maris, E., Schoffelen, J.M., 2011. FieldTrip: open source software for advanced analysis of MEG, EEG, and invasive electrophysiological data. Comput. Intell. Neurosci. 2011. doi:10.1155/2011/156869.
Opitz, A., Paulus, W., Will, S., Antunes, A., Thielscher, A., 2018. Determinants of the electric field during transcranial direct current stimulation. Neuroimage 109, 140–150. doi:10.1016/j.neuroimage.2015.01.033.
Pascual-Marqui, R.D., Michel, C.M., Lehmann, D., 1994. Low resolution electromagnetic tomography: a new method for localizing electrical activity in the brain. Int. J. Psychophysiol. 18 (1), 49–65. doi:10.1016/0167-8760(84)90014-X.
Pascual-Marqui, Roberto D, Pascual-Montano, A.D., Lehmann, D., Kochi, K., Esslen, M., Jancke, L., … Hirata, K., 2006. Exact low resolution brain electromagnetic tomography (eLORETA). Neuroimage 31 (Suppl 1).
Paz-Linares, D., Vega-Hernández, M., Rojas-López, P.A., Valdés-Hernández, P.A., Martínez-Montes, E., Valdés-Sosa, P.A., 2017. Spatio temporal EEG source imaging with the hierarchical bayesian Elastic Net and Elitist Lasso models. Front. Neurosci. 11 (NOV). doi:10.3389/fnins.2017.00635.
Paz-Linares, D, Gonzalez-Moreira, E, Areces-Gonzalez, A, Wang, Y, Li, M, Vega-Hernandez, M, Wang, Q, Bosch-Bayard, J, Bringas-Vega, ML, Martinez-Montes, E, Valdes–Sosa, MJ, 2023. Minimizing the distortions in electrophysiological source imaging of cortical oscillatory activity via Spectral Structured Sparse Bayesian Learning. Frontiers in Neuroscience 17, 978527.
Piastra, M.C., Nüßing, A., Vorwerk, J., Bornfleth, H., Oostenveld, R., Engwer, C., Wolters, C.H., 2018. The discontinuous Galerkin finite element method for solving the MEG and the combined MEG/EEG forward problem. Front. Neurosci. (FEB) 12. doi:10.3389/fnins.2018.00030.
Piastra, M.C., Nüßing, A., Vorwerk, J., Clerc, M., Engwer, C., Wolters, C.H., 2020. A comprehensive study on electroencephalography and magnetoencephalography sensitivity to cortical and subcortical sources. Hum. Brain Mapp. doi:10.1002/hbm.25272.
Pollitt, A., Hutchinson, C., 1987. Calibrating graded assessments: rasch partial credit analysis of performance in writing. Language Testing 4 (1), 72–92. doi:10.1177/026553228700400107.
Rahmouni, L., Adrian, S.B., Cools, K., Andriulli, F.P., 2019. Conforming discretizations of boundary element solutions to the electroencephalography forward problem. Comptes Rendus Physique 19 (1–2), 7–25. doi:10.1016/j.crhy.2018.02.002.
Reid, A.T., Headley, D.B., Mill, R.D., Sanchez-Romero, R., Uddin, L.Q., Marinazzo, D., … Biswal, B.B., 2019. Advancing functional connectivity research from association to causation. Nat. Neurosci. 22 (11), 1751–1760.
Riaz, U, Razzaq, FA, Gonzalez, AA, Linares, DP, Vega, ML, Sosa, PV, 2021. Statistically identifying and removing the spectral differences between EEG and MEG. Int. J. Psychophysiol. 168, S96–S97.
Riaz, U, Razzaq, FA, Hu, S, Valdés-Sosa, PA, 2021. Stepwise covariance-free common principal components (CF-CPC) with an application to neuroscience. Frontiers Neurosci 15, 750290.
Riaz, U., 2021. Transferal from EEG to MEG. Int. J. Psychophysiol. 168, S10.
Riera, J.J., Fuentes, M.E., 1998. Electric lead field for a piecewise homogeneous volume conductor model of the head. IEEE Trans. Biomed. Eng. 45 (6), 746–753. doi:10.1109/10.678609.
Schirner, M., Rothmeier, S., Jirsa, V.K., McIntosh, A.R., Ritter, P., 2015. An automated pipeline for constructing personalized virtual brains from multimodal neuroimaging data. Neuroimage 117, 343–357. doi:10.1016/j.neuroimage.2015.03.055.
Schrader, S., Westhoff, A., Piastra, M.C., Miinalainen, T., Pursiainen, S., Vorwerk, J., … Engwer, C., 2021a. DUNEuro - A software toolbox for forward modeling in bioelectromagnetism. PLoS ONE 16 (6 June), 1–21. doi:10.1371/journal.pone.0252431.
Schrader, S., Westhoff, A., Piastra, M.C., Miinalainen, T., Pursiainen, S., Vorwerk, J., … Engwer, C., 2021b. DUNEuro - A software toolbox for forward modeling in bioelectromagnetism. PLoS ONE 16 (6 June), 1–21. doi:10.1371/journal.pone.0252431.
Strang, G., Fix, G.J., .& Griffin, D.S. (.1974). *An analysis of the finite-element method*.
Tadel, F., Baillet, S., Mosher, J.C., Pantazis, D., Leahy, R.M., 2011. Brainstorm: a user-friendly application for MEG/EEG analysis. Comput. Intell. Neurosci. 2011. doi:10.1155/2011/879716.
Trujillo-Barreto, N.J., Aubert-Vázquez, E., Valdés-Sosa, P.A., 2004. Bayesian model averaging in EEG/MEG imaging. Neuroimage 21 (4), 1300–1319.
Turovets, S.I., Poolman, P., Salman, A., Malony, A.D., Tucker, D.M., 2008. Conductivity analysis for high-resolution EEG. 2008 Int. Conference on BioMed. Eng. Informatics 2, 386–393.
Valdes-Sosa, P.A., Sanchez-Bornot, J.M., Sotero, R.C., Iturria-Medina, Y., Aleman-Gomez, Y., Bosch-Bayard, J., … Ozaki, T., 2009. Model driven EEG/fMRI fusion of brain oscillations. Hum. Brain Mapp. 30 (9), 2701–2721. doi:10.1002/hbm.20704.
Van Veen, B.D., Van Drongelen, W., Yuchtman, M., Suzuki, A., 1997. Localization of brain electrical activity via linearly constrained minimum variance spatial filtering. IEEE Trans. Biomed. Eng. 44.
Vatta, F., Meneghini, F., Esposito, F., Mininel, S., Di Salle, F., 2010. Realistic and spherical head modeling for EEG forward problem solution: a comparative cortex-based analysis. Comput. Intell. Neurosci. 2010. doi:10.1155/2010/972060.
Vega, ML., Riaz, U., Razzaq, FA., Gonzalez, AA., Linares, DP., Sosa, PV., 2021. Auto-Q-CLF: A quick and reliable EEG lead field quality control for big databases. Int. J. Psychophysiol. 168, S183–S184.
Vinck, M., Perrenoud, Q., 2019. Layers of Rhythms—From Cortical Anatomy to Dynamics. Neuron 101 (3), 358–360.
Vladimirov, V.S., 1976. Equations of mathematical physics. Moscow Izdatel Nauka.
Vorwerk, J., JH, C., S, R., H, H., TR, K., CH, W, 2014. A guideline for head volume conductor modeling in EEG and MEG. NeuroImage, Epub 590–607. Retrieved from https://www.researchgate.net/publication/263514717_A_Guideline_for_Head_Volume_Conductor_Modeling_in_EEG_and_MEG?pli=1&loginT=IZYW2B93mXAeH1XtgtFHWbDm0DFIgzfM9WUn6xDgmD4*&uid=cad94631-51f5-49fd-aeae-075ae3b518c0&cp=re289_x_p23&ch=reg%0Apapers3://publicati .
Vorwerk, J., Oostenveld, R., Piastra, M.C., Magyari, L., Wolters, C.H., 2018a. The FieldTrip-SimBio pipeline for EEG forward solutions. Biomed. Eng. Online 17 (1), 37. doi:10.1186/s12938-018-0463-y.
Vorwerk, J., Oostenveld, R., Piastra, M.C., Magyari, L., Wolters, C.H., 2018b. The FieldTrip-SimBio pipeline for EEG forward solutions. Biomed. Eng. Online 17 (1). doi:10.1186/s12938-018-0463-y.
Vorwerk, J., Aydin, Ü., Wolters, C.H., Butson, C.R., 2019. Influence of head tissue conductivity uncertainties on EEG dipole reconstruction. Front. Neurosci. 13 (JUN), 1–17. doi:10.3389/fnins.2019.00531.
Vorwerk, J., Cho, J.-H., Rampp, S., Hamer, H., Knösche, T.R., .& Wolters, C.H. (.n.d.). *A Guideline for Head Volume Conductor Modeling in EEG and MEG*.
Windhoff, M., Opitz, A., Thielscher, A., 2013. Electric field calculations in brain stimulation based on finite elements: an optimized processing pipeline for the generation and usage of accurate individual head models. Hum. Brain Mapp. 34 (4), 923–935. doi:10.1002/hbm.21479.
Wipf, D., Nagarajan, S., 2009. A unified Bayesian framework for MEG/EEG source imaging. Neuroimage 44 (3), 947–966.
Wipf, D.P., Ramırez, R.R., Palmer, J.A., Makeig, S., Rao, B.D., 2006. Automatic Relevance Determination For Source Localization With MEG and EEG Data. University of California, San Diego Technical Report.

Wolters, C.H., Köstler, H., Möller, C., Härdtlein, J., Anwander, A., 2007. Numerical approaches for dipole modeling in finite element method based source analysis. Int. Congress Series 1300, 189–192. doi:10.1016/j.ics.2007.02.014.

Wu, M., Tam, H.P., Jen, T.-.H., 2016. Educational measurement for applied researchers. Educational Measurement for Applied Researchers doi:10.1007/978-981-10-3302-5.

Xie, Y., Yuan, J., Xinshan, X., Guan, X., 2001. Calculation of EEG problems with anisotropic conducting media by the finite volume method. IEEE Trans. Magn. 37 (5), 3749–3752. doi:10.1109/20.952705.

Yamaguchi, E., 2014. Finite element method. Bridge Eng. Handbook: Fundamentals, Second Edition 225–251. doi:10.1201/b15616.

Zucker, R., 1965. Elementary transcendental functions: logarithmic, exponential, circular and hyperbolic functions. Handbook of Mathematical Functions with Formulas, Graphs, and Mathematical Tables 65–94.